



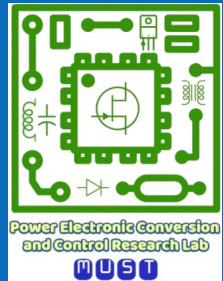
# Academic Oral Presentation

Title: Optimized Transient Modulation and Control Strategies for Bidirectional Dual-Active-Bridge DC-DC Converters

Presenter: Dr. SUN Chuan (孫川)

Institute: Macau University of Science and Technology (澳門科技大學)

Date: July 21, 2025





# Contents

- ▶ Introduction
- ▶ Overview of Existing Modulation and Control Strategies
- ▶ Optimal Transient SPS Modulation for NR-DABC
- ▶ Trajectory-Switching Modulation for SR-DABC
- ▶ Generalized Trajectory-Switching Modulation for DABC
- ▶ Conclusions



# On the Necessity of Improving IBDC's Dynamics

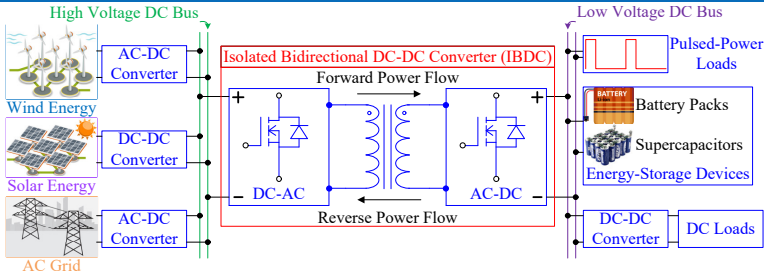


Figure 1: Distributed renewable energy generation and storage system.

## Why Does IBDC Require Fast Dynamics?

- Large uncertain and unpredictable **power flow fluctuations** induced by renewable energy sources.
- IBDCs are increasingly used in applications (e.g., **pulsed-power loads**) requiring fast responses.
- Fast responses allow the use of smaller output capacitors, thereby **reducing the filter size**.
- Existing control methods have shown their inability to achieve **fast** and **smooth** load transitions.

⇒ Further optimization of the dynamics and control design is necessary!



# Typical Topologies of DABC

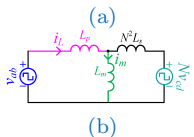
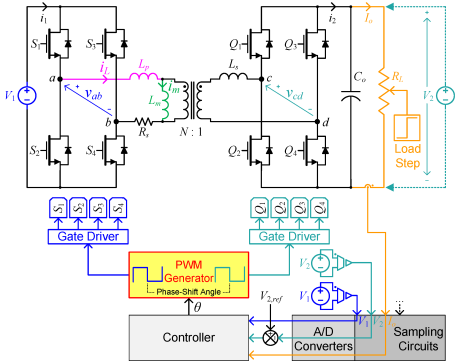


Figure 2: Circuit schematic of NR-DABC.

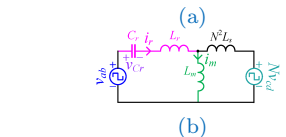
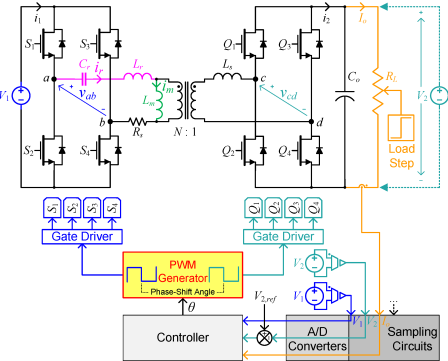


Figure 3: Circuit schematic of SR-DABC.

## Benefits

simple structure,  
galvanic isolation,  
high efficiency,  
high power density,  
flexibility of control,  
ease of modulation,  
wide ZVS range, etc.

## Basic Principles

controlling the shape  
of the high-frequency-  
link current is equiva-  
lent to controlling the  
direction and amount  
of the power flow be-  
tween the two sides.



# Roles of Controller and Transient Modulation

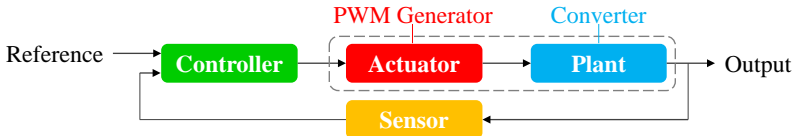


Figure 4: Relationship between actuator and controller.

In response to a load change (power adjustment), the current value of the control variable (i.e.,  $\theta[n]$ ) should be changed to the desired value (i.e.,  $\theta[n + 1] = \theta[n] + \Delta\theta$ ).

## Differences Between Control Design and Transient Modulation

- The controller determines the optimal control variables (i.e., phase-shift angles) to maintain a constant output voltage, according to the feedback information.
- The PWM generator (actuator) determines the switching sequences for driving power switches. (**It is the responsibility of PWM generator to specify the way to update the control variables.**)

⌚ As a result, both the controller and transient modulation determined by PWM generator can affect the dynamic performance of a closed-loop controlled DABC.



# Transient DC Offsets in NR-DABC

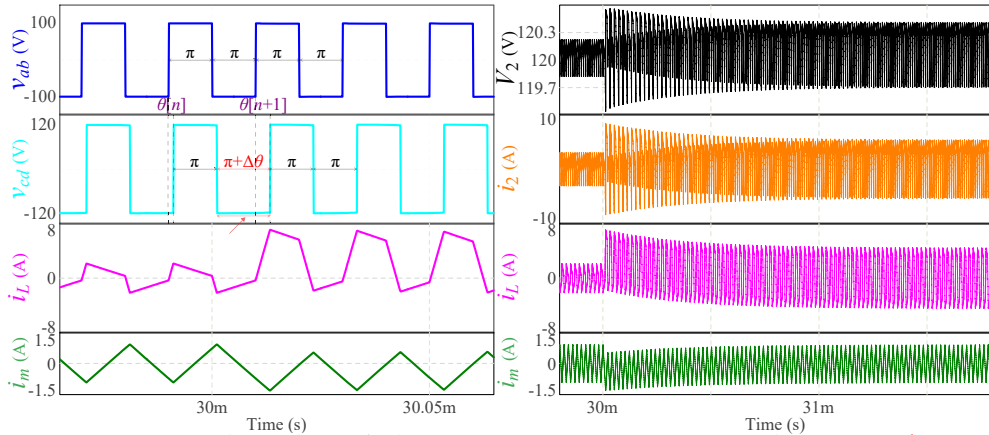


Figure 5: Transient waveforms of NR-DABC under **conventional transient phase-shift modulation (CTPSM)**.



risk of saturation in magnetic elements, triggering of protection, long settling time, etc.



# Transient Beat-Frequency Oscillations in SR-DABC

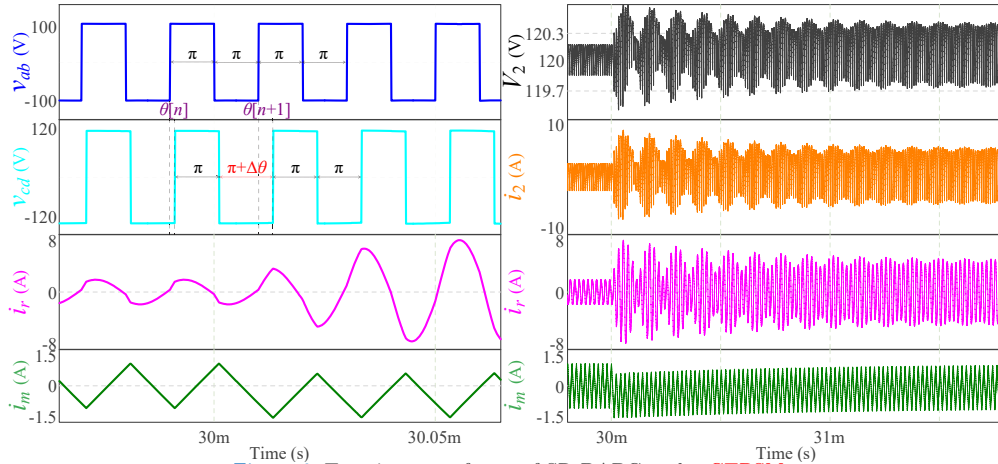


Figure 6: Transient waveforms of SR-DABC under CTPSM.



high voltage and current stresses, power device ageing and damage, long settling time, etc.



# Motivation

## Benefits of Using Fast and High-Gain Controller

Reduced Response Time, Lower Output Voltage Fluctuation, Smaller Steady-State Tracking Error, More Compact System Integration, etc.

## ⚠ Potential Problems Posed by CTPSM

A fast and high-gain controller can lead to abrupt and large variations in the control variables, thus producing severe transient dc offsets and oscillations under CTPSM.

### Motivation

#### ★ How to ensure a fast but smooth transition process?

⇒ The high-frequency-link current of DABC should be modulated and controlled properly!

⇒ This motivates our research to (1) gain a thorough understanding of DABC's transient behaviour and its relation to transient modulation, and (2) develop advanced transient modulation schemes for achieving ultra-fast, dc-offset-free, and oscillation-free dynamics.



# Objectives

## Objectives

- ① To better analyze and explain the causes of transient dc offsets generated in the magnetic elements of NR-DABC and HF transient oscillations generated in the resonant tank of SR-DABC.
- ② To investigate the fundamental relationships between various types of transient modulation schemes, and to attempt to establish a set of unified equations that can govern the existing schemes.
- ③ To propose new and more advanced transient modulation strategies for both NR-DABC and SR-DABC, and to examine their effects on fast closed-loop controlled DABCs when they are implemented in a cycle-by-cycle manner.
- ④ To compare the simulation and experimental results under different transient modulation strategies, and to find the optimal ones for NR-DABC and SR-DABC.
- ⑤ To offer systematic design approaches for developing transient modulation strategies, and to shed light on the general theory of optimizing the dynamics of DABCs.



# Contents

- ▶ Introduction
- ▶ Overview of Existing Modulation and Control Strategies
- ▶ Optimal Transient SPS Modulation for NR-DABC
- ▶ Trajectory-Switching Modulation for SR-DABC
- ▶ Generalized Trajectory-Switching Modulation for DABC
- ▶ Conclusions





# Optimized Steady-State Modulation Strategies

for Improving Conversion Efficiency

Outer Phase-shift Angle:  $\theta_2$

Inner Phase-shift Angles:  $\theta_1$  and  $\theta_3$

SPS Modulation:  $\theta_2 \neq 0$ ,  $\theta_1 = 0$ , and  $\theta_3 = 0$

DPS Modulation:  $\theta_2 \neq 0$ ,  $\theta_1 = 0$ , or  $\theta_3 = 0$

TPS Modulation:  $\theta_2 \neq 0$ ,  $\theta_1 \neq 0$ , and  $\theta_3 \neq 0$

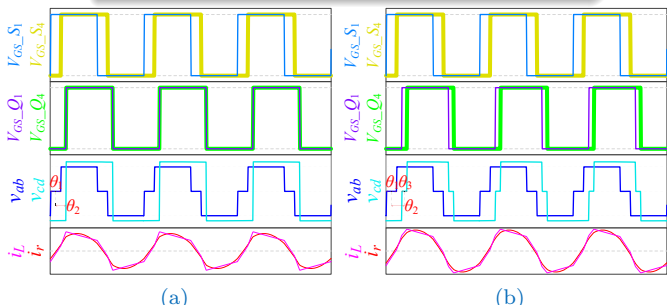


Figure 7: Typical steady-state waveforms of NR-DABC and SR-DABC under (a) DPS and (b) TPS modulation schemes.

## Efficiency Optimization Method

**Optimization Problem:** for a given power level, different combinations of  $\theta_1$ ,  $\theta_2$ , and  $\theta_3$  can be found under multi-phase-shift (MPS) modulation schemes for maximizing the overall efficiency [57]-[68].

**Optimization Objectives:** minimum root-mean-square (RMS) or peak-to-peak value for DABC's high-frequency-link current, low or zero backflow power, wide-range ZVS operation, etc.

**Optimization Methods:** Lagrange multipliers and Karush–Kuhn–Tucker (KKT) conditions [51],[57], particle swarm optimization (PSO) algorithm [62]-[64], genetic algorithm [65], artificial intelligence (AI) algorithm [66]-[68], etc.

# Optimized Transient Modulation Strategies (OTPSM)

for Eliminating Transient DC Offsets in NR-DABC



## Cause of Transient DC Offsets

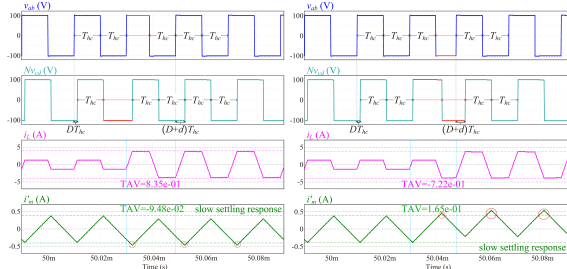
Any asymmetry in the inductor volt-second product will lead to magnetic flux imbalance that induces dc offsets, and hence the directly-adjusted transient switching pattern under CTPSM will lead to a monotonic increase in the volt-second product or flux linkage of the inductor during transient state.

## Basic Principle of OTPSM

To design specific switching sequences that can seamlessly modify the inductor current and achieve dynamic volt-second balance during transient state.

## Main Advantage of OTPSM

To directly update a large-amplitude phase-shift increment or decrement within about one switching cycle and to limit the inductor current.



(a)

(b)

Both Type-A [90]-[94] and Type-B OTPSM [94]-[96] strategies originate from “Relative Motion”.

**Drawbacks:** (1) serious transient dc offset and long settling time exist in  $i_m$ ; (2) designed transient pulse widths under Type-A and Type-B OTPSM strategies are related to the voltage gain  $M = NV_2/V_1$ .



# Optimized Transient Modulation Strategies (OTPSM)

for Eliminating Transient DC Offsets in NR-DABC

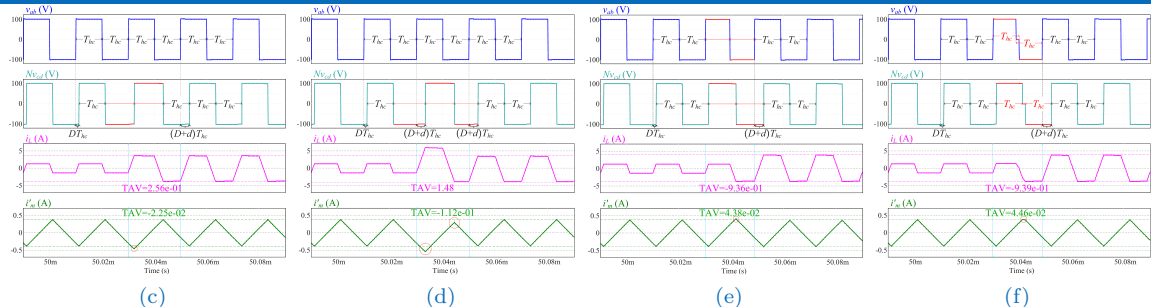


Figure 8: Simulated open-loop transient response of NR-DABC under different types of OTPSM strategies: (a) Type A<sub>1</sub> [90]. (b) Type B<sub>1</sub> [94]. (c) Type C<sub>1</sub> [97]. (d) Type D<sub>1</sub> [98]. (e) Type E<sub>1</sub> [100]. (f) Type F<sub>1</sub> [100].

Type-C and Type-E OTPSM strategies generate two equal-width transient pulses by consecutively moving two edges of  $v_{ab}$  and/or  $v_{cd}$ , while Type-D OTPSM continuously generates three unequal-width transient pulses in  $v_{cd}$ . Type-F OTPSM introduces zero-voltage durations into  $v_{ab}$  and/or  $v_{cd}$ .

**Drawbacks:** All Type-C to Type-F OTPSM strategies can lead to overshoots/undershoots in  $i_m$ , and the average values of both  $i_L$  and  $i_m$  during transient state are not zero.



# Optimized Transient Modulation Strategies

for Eliminating Transient Oscillations in SR-DABC

How to effectively modify the transient trajectories of resonant waveforms of SR-DABC?

## Non-linear Dynamics of SR-DABC

Unlike the piecewise-linear inductor current in NR-DABC that can directly reach a specific value by linearly adjusting the turn-on and turn-off pulse widths of some power switches, the trajectory of the non-linear resonant current in SR-DABC cannot be easily modified to follow the changes in pulse durations instantaneously due to the inertia of the resonant tank. Therefore, none of the OTPSM strategies developed for NR-DABC can be applied to suppress the transient oscillations in SR-DABC.

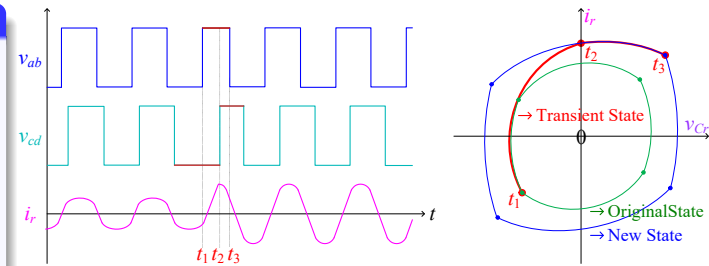


Figure 9: Principle diagram of a trajectory-prediction-based transient modulation strategy for SR-DABC [109].

Recently, four OTPSM strategies were proposed in [109]-[111] for eliminating transient oscillations in SR-DABC.

**Drawbacks:** (1) closed-form expressions are not available; (2) they require rich feedback information and several high-bandwidth sensors for trajectory planning and computation.



# Disadvantages of Different Control Methods

## Pure PI Control [118]-[123]

The interaction between the two tuning parameters makes it challenging to simultaneously achieve fast and stable performance over the whole operating range.

## Pre-Calculated Feed-Forward Control [124]

A lookup table is used to decouple the complex relationship between phase-shift angle and load current, but the control performance relies on the difference between actual and nominal circuit parameters.

## Virtual Direct Power Control [125]

Although it is effective in cancelling the effects of circuit parameters, its performance degrades significantly at light-load conditions.

## Current-Mode Control [126]-[129]

## Natural-Switching-Surface Control [130]

## Deadbeat Current Control [131]

They are not desirable solutions because the high-frequency-link current of DABC must be sampled by costly high-bandwidth sensors at a high sampling rate (i.e., at least twice the switching frequency).

## Disturbance-Observer Control [132]-[133]

## Sliding-Mode Control [134]

## Model Predictive Control [9],[41]-[45]

In exchange for fast transient response, the controller's gain and bandwidth must be increased. The control variables (i.e., phase-shift angles) will undergo large-magnitude changes under CTPSM, thus resulting in large transient dc offsets and oscillations.

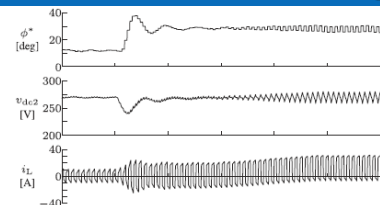


# How to Achieve Optimal Dynamic Performance?

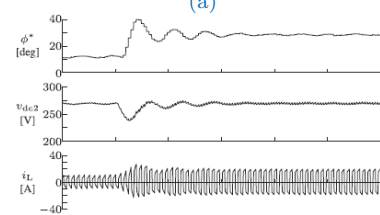
**New Solution:** Sensorless OTPSM+Fast Controller (e.g., MPC)

## ❗ Significant Limitations of Existing OTPSM Schemes

- ➊ The inner links between different OTPSM schemes are unclear. Existing OTPSM strategies developed for NR-DABC cannot achieve complete transient dc-offset elimination, and there is no easy-to-implement OTPSM for SR-DABC.
- ➋ All previous OTPSM strategies except [100] have only been validated in open-loop conditions, and hence their OTPSM algorithms (transient pulse widths) must be pre-calculated.
- ➌ A much-debated question is whether such OTPSM strategies can truly bring about positive effects on improving the dynamics of closed-loop controlled DABC. A pure PI controller typically suffers from a trade-off between response time and stability margin. As demonstrated in [100], if PI controller's gain is too high, the system can become unstable.



(a)



(b)

Figure 10: Experimental transient response of NR-DABC under **single-voltage-loop PI controller** with (a) CTPSM and (b) Type  $F_1$  OTPSM [100].



# Contents

- ▶ Introduction
- ▶ Overview of Existing Modulation and Control Strategies
- ▶ Optimal Transient SPS Modulation for NR-DABC
- ▶ Trajectory-Switching Modulation for SR-DABC
- ▶ Generalized Trajectory-Switching Modulation for DABC
- ▶ Conclusions





# Primary-Referred Equivalent Circuits of NR-DABC

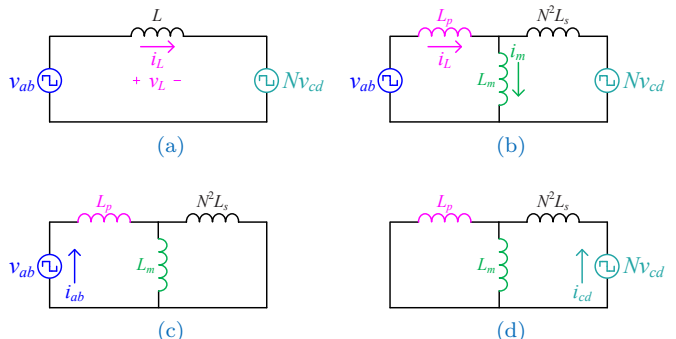


**Figure 11:** Primary-referred equivalent circuits of NR-DABC.  
 (a) Ideal equivalent circuit. (b) T-model equivalent circuit. Applying superposition principle. (c) Individual contribution due to  $v_{ab}$ . (d) Individual contribution due to  $Nv_{cd}$ .

Magnetizing Inductance:  $L_m \gg L$

Total Equivalent Series Inductance:  $L = L_p + N^2 L_s$

## Applying Superposition Principle

$$i_L = i_{ab} - \frac{L_m}{L_m + L_p} i_{cd} \approx i_{ab} - i_{cd} \quad (1)$$

$$i_m = \frac{N^2 L_s}{L_m + N^2 L_s} i_{ab} + \frac{L_p}{L_m + L_p} i_{cd} \quad (2)$$

## Steady-State Power Transfer Model

$$\begin{aligned} P &= \frac{1}{2T_{hc}} \int_0^{2T_{hc}} v_{ab}(t) i_L(t) dt \\ &\approx \frac{NV_1 V_2 T_{hc} D(1 - D)}{L} \end{aligned} \quad (3)$$



During Transient State

$D$   $\xrightarrow{\text{needs to be adjusted to}}$   $D + d$



# Unified Transient-Modulation Framework for NR-DABC

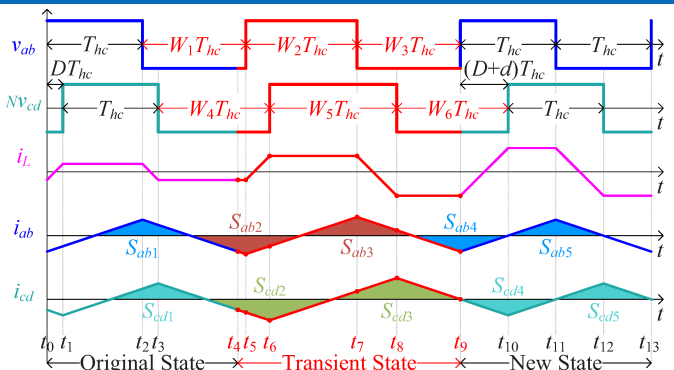


Figure 12: Unified framework of OTPSM strategies for NR-DABC.

- Constraint ①: The time interval  $t_{10} - t_9$  should be equal to  $(D + d)T_{hc}$ .  $\Rightarrow W_1 + W_2 + W_3 + d = W_4 + W_5 + W_6$
- Constraint ②:  $i_L(t_9) = i_L(t_{13})$ .  $\Rightarrow 0 = (2 - 2W_1 + 2W_2 - 2W_3) + (2W_1 + 2W_2 + 2W_3 - 4W_5 - 2 + 2d)M$

## General Solution of OTPSM

All the Type-A to Type-E OTPSM strategies fulfill the two constraints.

- :( W<sub>1</sub> ~ W<sub>6</sub> cannot be decoupled from M.
- :( Eliminating the dependence of M yields a general solution for sensorless OTPSM:

$$\begin{cases} 1 + W_2 = W_1 + W_3 \\ 1 + W_5 = W_4 + W_6 \\ 2W_2 + d = 2W_5. \end{cases} \quad (4)$$

## Minimizing Transient DC Offsets

- :( The average values of  $i_{ab}$  and  $i_{cd}$  are zero (symmetric about the horizontal axis).

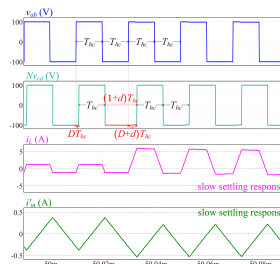
$$\begin{cases} W_1 = W_3 = (1 + W_2)/2 \\ W_4 = W_6 = (1 + W_5)/2 \\ 2W_2 + d = 2W_5 \end{cases} \quad (5)$$



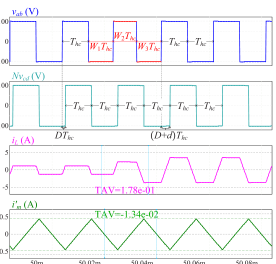
# Two Simple Particular Solutions of (5) $\Rightarrow$ SS-OTPSM

☺ Type-I SS-OTPSM ( $v_{cd}$  is unmodulated):

$$\begin{cases} W_1 = W_3 = 1 - \frac{d}{4} \\ W_2 = 1 - \frac{d}{2} \\ W_4 = W_5 = W_6 = 1 \end{cases} \quad (6)$$



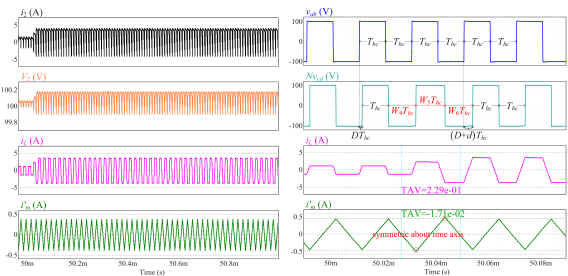
(a)



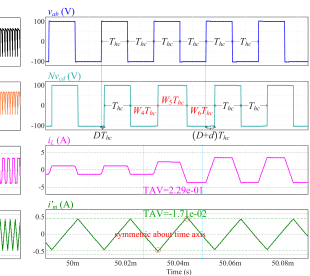
(b)

☺ Type-II SS-OTPSM ( $v_{ab}$  is unmodulated):

$$\begin{cases} W_1 = W_2 = W_3 = 1 \\ W_4 = W_6 = 1 + \frac{d}{4} \\ W_5 = 1 + \frac{d}{2} \end{cases} \quad (7)$$



(c)



(d)

**Figure 13:** Simulated open-loop transient response for an increase in the phase-shift ratio under CTPSM and SS-OTPSM strategies. (a) Transient waveforms under CTPSM. (b) Transient waveforms under Type-I SS-OTPSM. (c) Zoomed-out transient waveforms of  $i_2$ ,  $V_2$ ,  $i_L$ , and  $i_m$  under Type-I SS-OTPSM. (d) Transient waveforms under Type-II SS-OTPSM.



# Parameter Sensitivity Analysis for Type-I SS-OTPSM

😊 SS-OTPSM (6) is always effective to eliminate transient dc offsets under different circuit parameters.

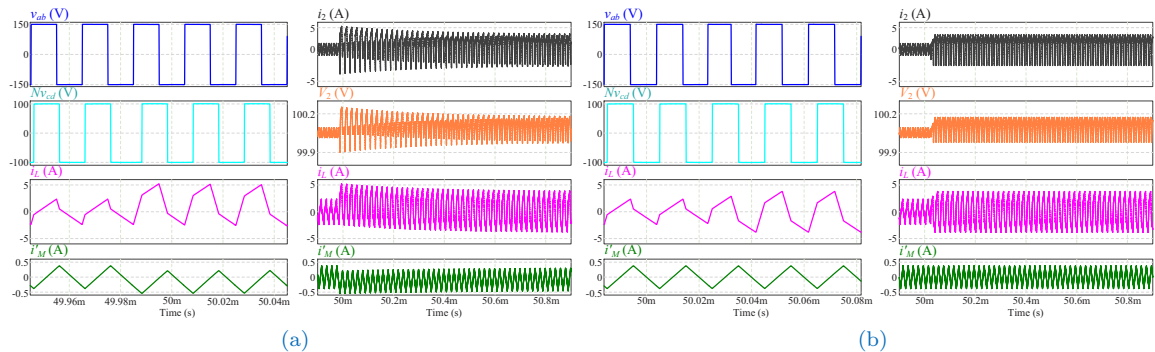


**Figure 14:** Parameter sensitivity analysis for Type-I SS-OTPSM. Simulated open-loop transient response under (a) CTPSM and (b) Type-I SS-OTPSM. The simulation parameters are as follows:  $f_s = 50$  kHz,  $V_1 = 150$  V,  $V_2 = 100$  V,  $L_p = 150$   $\mu$ H,  $L_s = 1.70$   $\mu$ H,  $L_m = 650$   $\mu$ H, and the phase-shift ratio is changed from  $\frac{1}{9}$  to  $\frac{1}{3}$ .



# Performance of SS-OTSPSM

**Table 1:** Main Features of Different OTSPSM Strategies for NR-DABC.

Type	DOF Reference	W1	W2	W3	W4	W5	W6	Sensorless Complexity	CE <sup>†</sup>
CTPSM	1	—	1	1	1 + d	1	1	Yes	★ No
A <sub>1</sub> OTSPSM	2 [90]	1	$1 - \frac{dM}{M+1}$	1	$1 + \frac{d}{M+1}$	1	1	No	★★★ No
A <sub>2</sub> OTSPSM	2 [91]	1	1	$1 - \frac{dM}{M+1}$	1	$1 + \frac{d}{M+1}$	1	No	★★★ No
A <sub>3</sub> OTSPSM	2 [91]	1	$1 - \frac{dM}{M-1}$	1	1	$1 - \frac{d}{M-1}$	1	No	★★★ No
A <sub>4</sub> OTSPSM	2 [91]	1	1	$1 - \frac{dM}{M-1}$	1	1	$1 - \frac{d}{M-1}$	No	★★★ No
A <sub>5</sub> OTSPSM	2 [92]	1	1	1	$1 + \frac{d}{M+1}$	$1 + \frac{dM}{M+1}$	1	No	★★★ No
A <sub>6</sub> OTSPSM <sup>§</sup>	2 [93]	1	1	$1 - \frac{d+2}{M+1}$	1	$1 + \frac{(d+2)M}{M+1}$	1	No	★★★★ No
A <sub>7</sub> OTSPSM	2 [94]	$1 - \frac{dM}{M-1}$	1	1	$1 - \frac{d}{M-1}$	1	1	No	★★★ No
B <sub>1</sub> OTSPSM	3 [94]	1	1	$1 - d$	1	$1 + \frac{d}{2M}$	$1 - \frac{d}{2M}$	No	★★★★ No
B <sub>2</sub> OTSPSM	3 [94]	1	$1 + \frac{dM}{2}$	$1 - \frac{dM}{2}$	1	1 + d	1	No	★★★★ No
B <sub>3</sub> OTSPSM	3 [95]	$1 + \frac{ D+d +D}{2}$	$1 - \frac{ D+d -D}{2}$	1	1	$1 -  D+d $	1	No	★★★★ No
B <sub>4</sub> OTSPSM	3 [96]	$1 + \frac{d}{2M}$	$1 - \frac{d}{2M}$	1	1 + d	1	1	No	★★★★ No
B <sub>5</sub> OTSPSM	3 [96]	$1 - \frac{d}{2M}$	$1 + \frac{d}{2M}$	1	1	1 + d	1	No	★★★★ No
C <sub>1</sub> OTSPSM	2 [97]	1	1	1	$1 + \frac{d}{2}$	$1 + \frac{d}{2}$	1	Yes	★ IE <sup>‡</sup>
C <sub>2</sub> OTSPSM	2 [94]	$1 - \frac{d}{2}$	$1 - \frac{d}{2}$	1	1	1	1	Yes	★ IE <sup>‡</sup>
D <sub>1</sub> OTSPSM	3 [98]	1	1	1	1 + d	$1 + \frac{d}{2}$	$1 - \frac{d}{2}$	Yes	★★ IE <sup>‡</sup>
D <sub>2</sub> OTSPSM	3 [99]	1	1	1	$1 + \frac{d(d-2D+4)}{4(d+2)}$	$1 + \frac{d}{2}$	$1 + \frac{d(d+2D)}{4(d+2)}$	Yes	★★ IE <sup>‡</sup>
E <sub>1</sub> OTSPSM	4 [100]	1	$1 - \frac{d}{4}$	$1 - \frac{d}{4}$	1	$1 + \frac{d}{4}$	$1 + \frac{d}{4}$	Yes	★★★ IE <sup>‡</sup>
E <sub>2</sub> OTSPSM <sup>§</sup>	4 [97]	$1 - \frac{D+d}{2}$	$1 - \frac{D+d}{2}$	1	$1 - \frac{D}{2}$	$1 - \frac{D}{2}$	1	Yes	★★★★ IE <sup>‡</sup>
F <sub>1</sub> OTSPSM	6 [100]	—	—	—	—	—	—	Yes	★★★★ IE <sup>‡</sup>
I-SS-OTSPSM	3 Proposed	$1 - \frac{d}{4}$	$1 - \frac{d}{2}$	$1 - \frac{d}{4}$	1	1	1	Yes	★ Yes
II-SS-OTSPSM	3 Proposed	1	1	1	$1 + \frac{d}{4}$	$1 + \frac{d}{2}$	$1 + \frac{d}{4}$	Yes	★ Yes

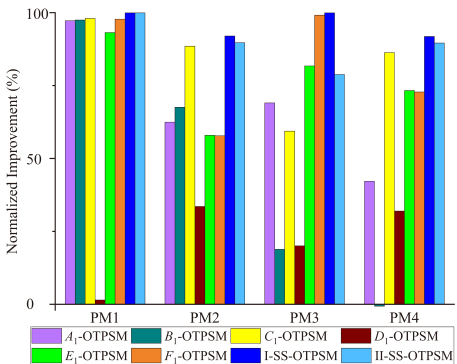


**Figure 15:** Performance evaluation of the OTSPSM strategies in open-loop simulations.

**PM1:** maximum overshoot of the peak amplitude of  $i_L$ .

**PM2:** absolute value of the transient dc offset of  $i_L$ .

**PM3:** maximum overshoot of the peak amplitude of  $i_m'$ .

**PM4:** absolute value of the transient dc offset of  $i_m'$ .



# Conventional MPC Design

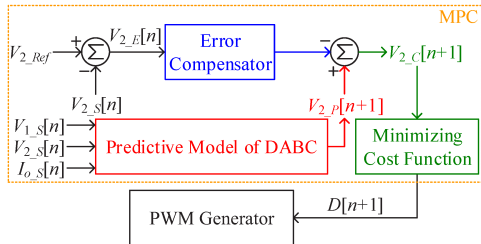


Figure 16: Conceptual block diagram of MPC.

Although different MPCs have been developed for NR-DABC, they can be generally depicted by Fig. 16. The major differences between the existing MPC schemes lie in the predictive model, error compensator and cost function.

A simple scheme [41]: one-step prediction + PI compensator + quadratic cost function.

## Conventional MPC [41]

- ① The dynamic behavior of  $V_2$  is described by

$$C_o \frac{dV_2}{dt} = \bar{i}_2 - I_o = \frac{\textcolor{red}{P}}{V_2} - I_o = \frac{NV_1 T_{hc} D(1 - D)}{L} - I_o \quad (8)$$

- ② Discretizing (8) using forward Euler approximation,

$$V_{2\_P}[n+1] \approx V_{2\_S}[n] + 2T_{hc} V_2'[n] \quad (9)$$

- ③ The cost function  $J$  is defined as

$$J = [V_{2\_Ref} - V_{2\_C}[n+1]]^2 \quad (10)$$

- ④ Minimizing  $J$  yields the optimal phase-shift ratio,

$$D[n+1] = \frac{1}{2} \left( 1 - \sqrt{1 - \frac{4K_2}{K_1}} \right) \quad (11)$$

$$K_1 = \frac{2NT_{hc}^2 V_{1\_S}[n]}{LC_o} \quad (12)$$

$$K_2 = 2T_{hc} I_{o\_S}[n]/C_o + V_{2\_E}[n] + (K_p V_{2\_E}[n] + K_i \sum_{\tau=0}^n V_{2\_E}[\tau]) \quad (13)$$

$$= 2T_{hc} I_{o\_S}[n]/C_o + (\textcolor{blue}{K}_p^* V_{2\_E}[n] + K_i \sum_{\tau=0}^n V_{2\_E}[\tau]) \quad (13)$$

$$K_p^* = K_p + 1 \quad (14)$$



# Enhanced MPC (EMPC) Design

A major problem with conventional predictive model is that the output/transmission power  $P$  (3) is derived based on steady-state waveforms; hence it cannot accurately predict the average power transferred during transient state.

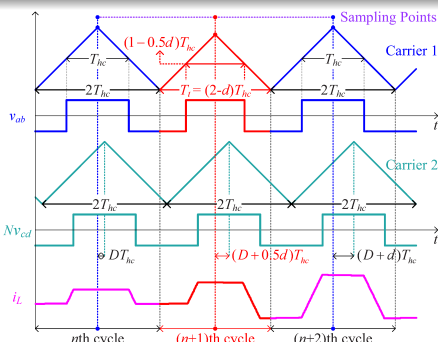


Figure 17: Implementation of Type-I SS-OTPSM.

## EMPC for SS-OTPSM

Average power under SS-OTPSM over the  $(n+1)^{th}$  cycle is given by,

$$\begin{aligned} P^* &= \frac{1}{(2-d)T_{hc}} \int_0^{(2-d)T_{hc}} v_{ab}(t)i_L(t)dt \\ &= \frac{NV_1V_2T_{hc}(8d-9d^2+16D-24Dd-16D^2)}{4(2-d)L} \end{aligned} \quad (15)$$

Refined the optimal phase-shift ratio  $D^*[n+1]$  employing EMPC is given by,

$$\begin{aligned} D^*[n+1] &= D[n] + d^* = \frac{(4-3D[n])K_1+2K_2}{9K_1} \\ &\quad - \frac{2\sqrt{4(1+3D[n])K_1^2-2(7+6D[n])K_1K_2+K_2^2}}{9K_1} \end{aligned} \quad (16)$$

😊 (16) gives a more accurate prediction of the optimal phase-shift ratio for SS-OTPSM, compared to (11).



## Selection of Control Parameters

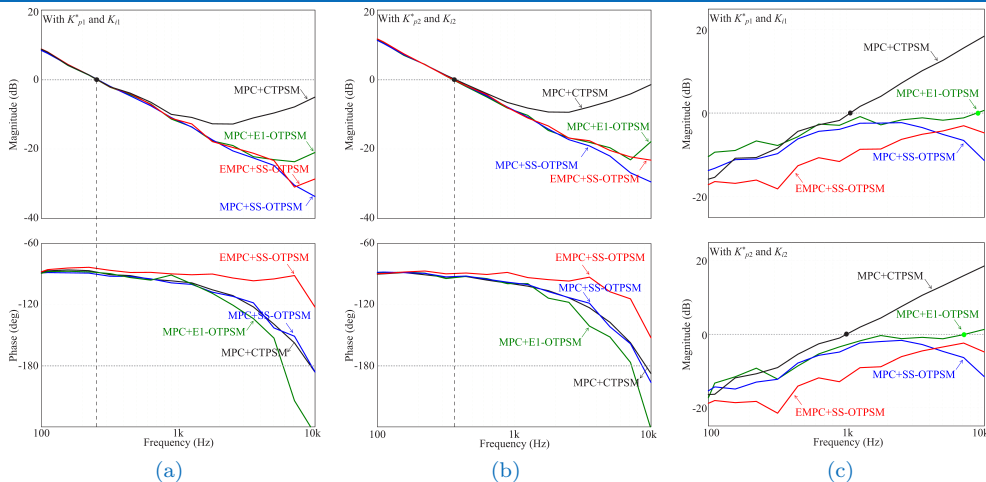


**Figure 18:** Simulated loop gains and closed-loop output impedances under different systems. (a) Loop gains with  $K_{p1}^* = 0.07$  and  $K_{i1} = 0.3$ . (b) Loop gains with  $K_{p2}^* = 0.1$  and  $K_{i2} = 0.5$ . (c) Closed-loop output impedances.



# Closed-Loop Simulations of Different MPC Systems

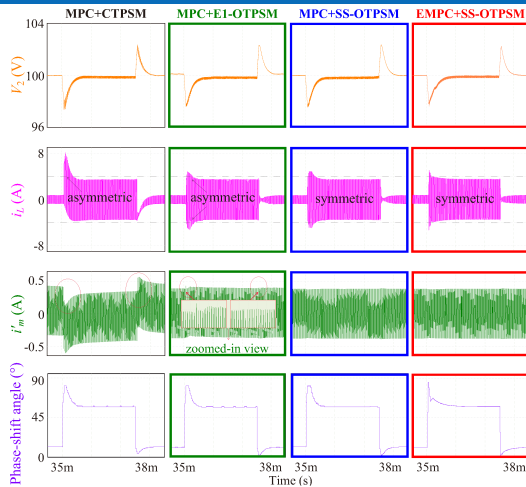


**Figure 19:** Simulated closed-loop transient responses of different MPC systems for step-load changes between 25% and 95% of the full load with  $K_{p2}^*$  and  $K_{i2}$ .

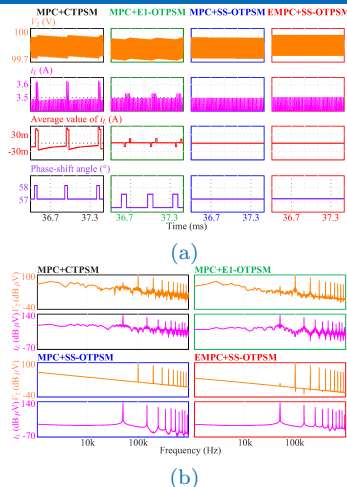


**Figure 20:** (a) Simulated steady-state waveforms at heavy loads. (b) FFT spectrum analysis.



# Closed-Loop Simulations Under LCFF Control

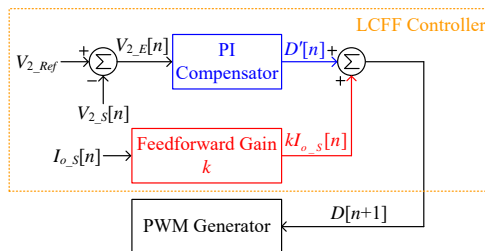


Figure 21: Block diagram of LCFF control Scheme.

## Load-Current Feed-Forward (LCFF) Control Scheme Introduced in [125]

If  $V_2_S[n]$  is far from  $V_2_{Ref}$ : Feed-Forward Path

If  $V_2_E[n]$  is close to 0: PI Compensator

$$D[n+1] = D'[n] + kI_{o,S}[n]$$

SS-OTPSM is compatible with most controllers.

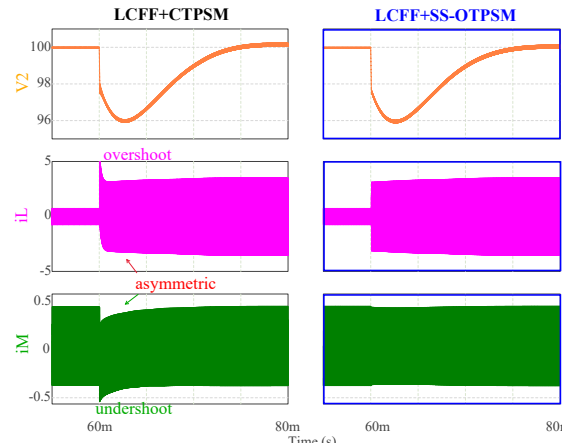


Figure 22: Simulated closed-loop transient responses under LCFF controller plus different transient modulation strategies. (The proportional and integral coefficients are chosen as 0.45 and 0.008, and the feed-forward ratio  $k$  is chosen as 24.)



# Experimental Setup of NR-DABC

Table 2: Circuit Parameters and Specifications of NR-DABC.

Symbol	Parameter Description	Value or Part Type
$P_{max}$	Rated Power	250 W
$V_1$	Input Voltage	100 V
$V_2$	Output Voltage	100 V
$C_o$	Output Capacitance	47 $\mu$ F
$R_L$	Load Resistance	150/43 $\Omega$
$N : 1$	Transformer Ratio	1 : 1
$L_m$	Magnetizing Inductance	650 $\mu$ H
$R_m$	ESR of $L_m$	260 m $\Omega$
$L_p$	Primary Inductance	92 $\mu$ H
$R_p$	ESR of $L_p$	211 m $\Omega$
$L_s$	Secondary Inductance	1.7 $\mu$ H
$S_x \sim Q_x$	Power Switches	UnitedSiC UJC06505K
$f_s$	Switching Frequency	50 kHz
–	Dead Time	250 ns
–	Voltage Sensing Circuit	Resistive Voltage Divider
–	Current Sensor	LEM LA 55-P
–	Microprocessor	TI TMS320F28335

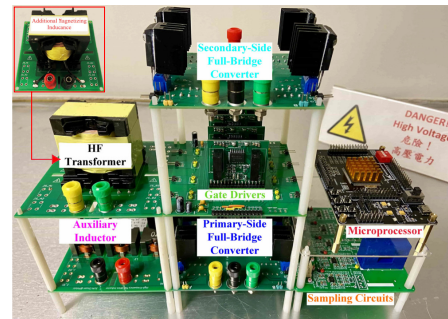


Figure 23: Photograph of the NR-DABC prototype.

- In open-loop tests: both terminals of are connected with dc voltage sources, and the phase-shift ratio is changed by a HMI software.
- In closed-loop tests: the output terminal is connected to variable resistive loads, and MPC (or EMPC) determines the phase-shift ratio.



# Open-Loop Tests #1 CTPSM

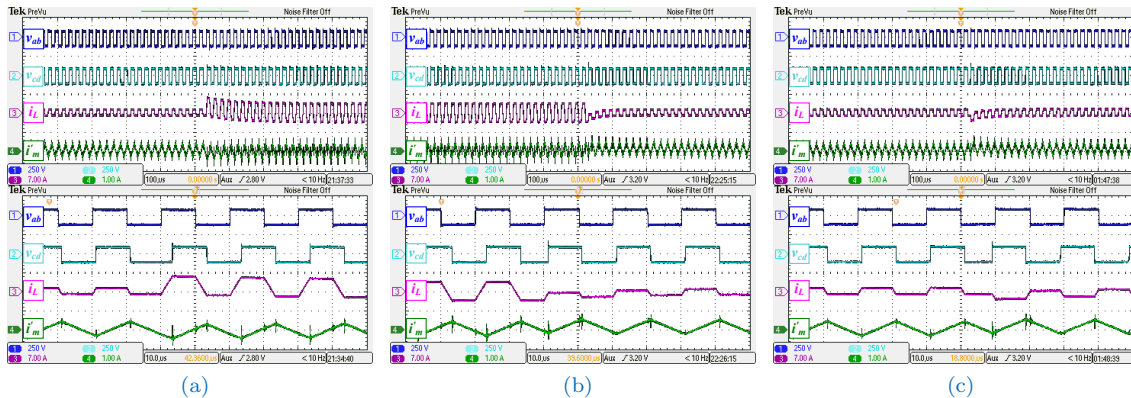
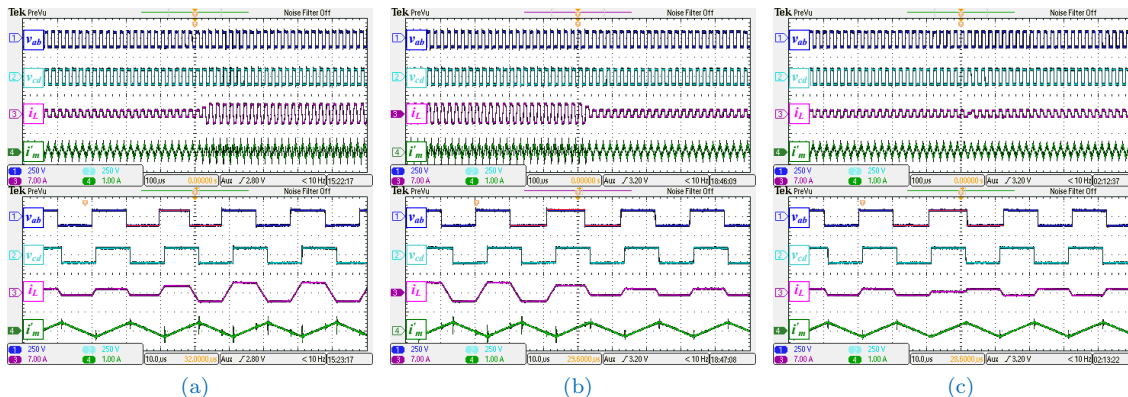


Figure 24: Open-loop experimental results under CTPSM. (a) The phase-shift ratio is changed from  $\frac{1}{9}$  to  $\frac{1}{3}$ . (b) The phase-shift ratio is changed from  $\frac{1}{3}$  to  $\frac{1}{9}$ . (c) The phase-shift ratio is changed from  $\frac{1}{9}$  to  $-\frac{1}{9}$ .



Open-Loop Tests #2 Proposed SS-OTPSM



**Figure 25:** Open-loop experimental results under the proposed SS-OTPSM. (a) The phase-shift ratio is changed from  $\frac{1}{9}$  to  $\frac{1}{3}$ . (b) The phase-shift ratio is changed from  $\frac{1}{2}$  to  $\frac{1}{6}$ . (c) The phase-shift ratio is changed from  $\frac{1}{6}$  to  $-\frac{1}{6}$ .



# Open-Loop Tests #3 Performance Evaluation

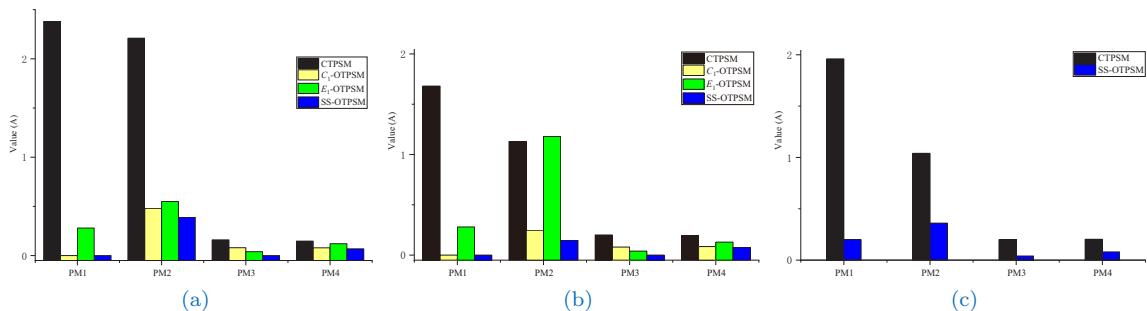


**Figure 26:** Performance evaluation of different transient modulation strategies in open-loop experiments. (a) For an increase in the phase-shift ratio from  $\frac{1}{9}$  to  $\frac{1}{3}$ . (b) For a decrease in the phase-shift ratio from  $\frac{1}{3}$  to  $\frac{1}{9}$ . (c) The phase-shift ratio is changed from  $\frac{1}{9}$  to  $-\frac{1}{9}$ .

- SS-OTPSM performs better than CTPSM and the other two OTPSM strategies (Type- $C_1$  and Type- $E_1$ ) due to its capability in further suppressing transient dc offsets in both  $i_L$  and  $i_m$  simultaneously.



# Closed-Loop Tests #1

(a) MPC+CTPSM (b) MPC+SS-OTPSM (c) EMPC+SS-OTPSM

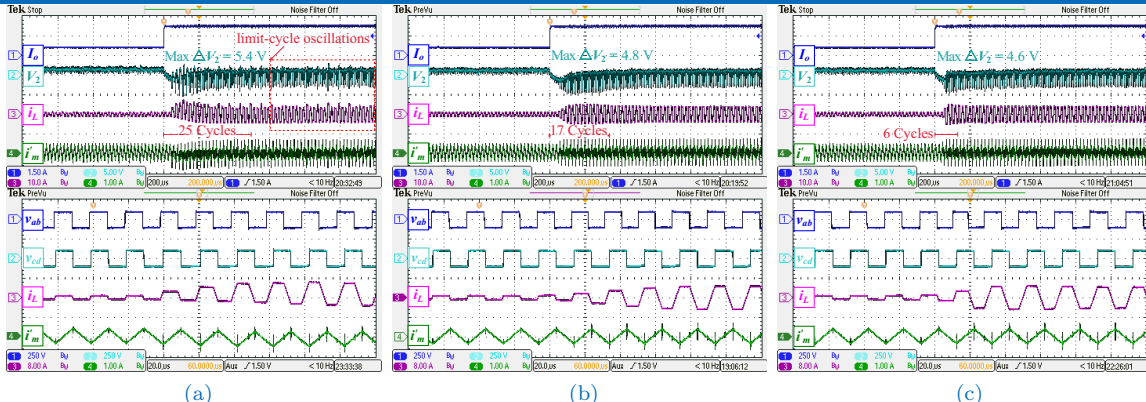


Figure 27: Experimental closed-loop transient responses for a step change in the load with  $\{K_{p2}^*=0.1, K_{i2}=0.5\}$ .

- ☹ MPC+CTPSM leads to the largest output voltage deviation, longest settling time, and excessive overshoots and transient dc offsets in both  $i_L$  and  $i_m$ .
- ☺ Under EMPC+SS-OTPSM, the settling times can be significantly reduced to 6-8 cycles with no obvious increase in the overshoot of  $i_L$  and  $i_m$ , and the output voltage deviation is also the smallest.



## Closed-Loop Tests #2

(a) MPC+CTPSM (b) MPC+SS-OTPSM (c) EMPC+SS-OTPSM

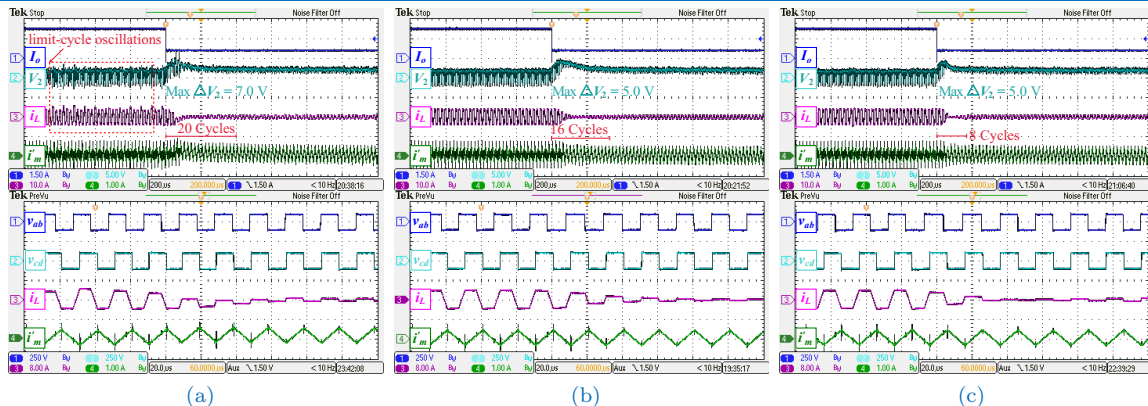
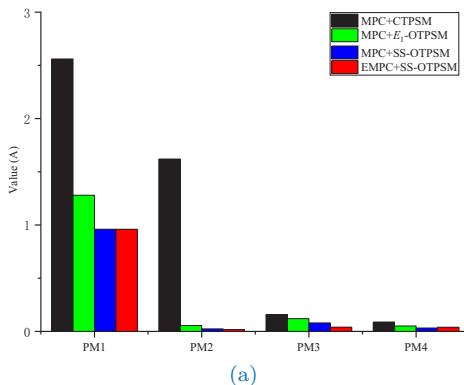


**Figure 28:** Experimental closed-loop transient responses for a step change in the load with  $\{K_{n2}^*=0.1, K_{i2}=0.5\}$ .

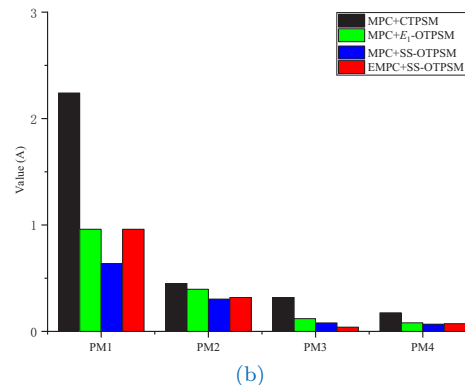
- The small-amplitude limit-cycle oscillations in the steady-state waveforms under MPC+CTPSM are caused by the presence of residual transient dc offsets, which can be avoided under MPC+SS-OTPSM and EMPC+SS-OTPSM as SS-OTPSM can achieve complete elimination of all transient dc offsets.



# Closed-Loop Tests #3 Performance Evaluation ( $K_{p2}^*$ & $K_{i2}$ )



(a)



(b)

Figure 29: Performance evaluation of closed-loop experiments. (a) Load step-up transition with  $\{K_{p2}^* = 0.10, K_{i2} = 0.5\}$ . (b) Load step-down transition with  $\{K_{p2}^* = 0.10, K_{i2} = 0.5\}$ .

- ☺ MPC+SS-OTPSM outperforms MPC+CTPSM and MPC+E<sub>1</sub>-OTPSM in the four indexes.
- ☺ With similar overshoots or undershoots in  $i_L$  and  $i_m$  compared with MPC+SS-OTPSM, EMPC+SS-OTPSM enables an optimal transient performance with fastest dynamics and best waveform quality.



# Contents

- ▶ Introduction
- ▶ Overview of Existing Modulation and Control Strategies
- ▶ Optimal Transient SPS Modulation for NR-DABC
- ▶ Trajectory-Switching Modulation for SR-DABC
- ▶ Generalized Trajectory-Switching Modulation for DABC
- ▶ Conclusions





# Steady-State Analysis of SPS-Modulated SR-DABC

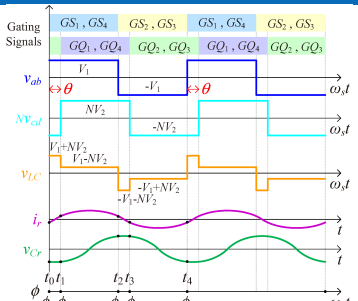


Figure 30: Time-domain waveforms.

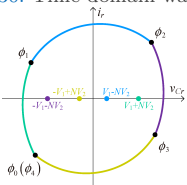


Figure 31: State-plane diagram.

## Time-Domain Analysis of Steady-State SPS Modulation

The  $L_r-C_r$  tank is excited by a multi-level voltage  $v_{LC} = v_{ab} - Nv_{cd}$ .

Applying Kirchhoff's voltage law (KVL) and symmetrical characteristics, the analytical expressions of  $i_r$  and  $v_{Cr}$ :

$$i_r\left(\frac{\phi}{\omega_s}\right) = i_r\left(\frac{\phi_i}{\omega_s}\right) \cos \frac{\phi - \phi_i}{F} + \frac{v_{LC} - v_{Cr}\left(\frac{\phi_i}{\omega_s}\right)}{Z_r} \sin \frac{\phi - \phi_i}{F} \quad (17)$$

$$v_{Cr}\left(\frac{\phi}{\omega_s}\right) = v_{LC} \cdot \left(1 - \cos \frac{\phi - \phi_i}{F}\right) + v_{Cr}\left(\frac{\phi_i}{\omega_s}\right) \cos \frac{\phi - \phi_i}{F} + Z_r \cdot i_r\left(\frac{\phi_i}{\omega_s}\right) \sin \frac{\phi - \phi_i}{F} \quad (18)$$

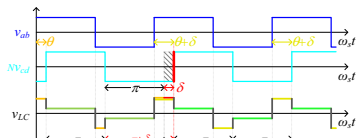
The values of  $i_r(\phi_i/\omega_s)$  and  $v_{Cr}(\phi_i/\omega_s)$  at different points  $\phi_i$  can be solved exactly. For example,

$$i_r\left(\frac{\phi_0}{\omega_s}\right) = \frac{1}{Z_r} \left[ NV_2 \sec\left(\frac{\pi}{2F}\right) \sin\left(\frac{\pi - 2\theta}{2F}\right) - V_1 \tan\left(\frac{\pi}{2F}\right) \right] \quad (19)$$

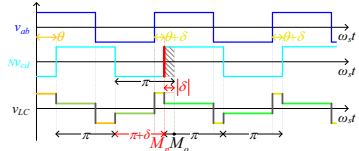
$$v_{Cr}\left(\frac{\phi_0}{\omega_s}\right) = NV_2 \left[ 1 - \cos\left(\frac{\theta}{F}\right) - \sin\left(\frac{\theta}{F}\right) \tan\left(\frac{\pi}{2F}\right) \right] \quad (20)$$



# Simulated Open-Loop Results Under CTPSM

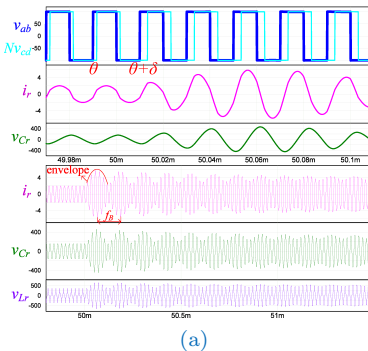


(a)

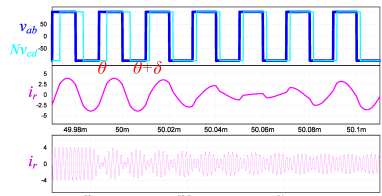


(b)

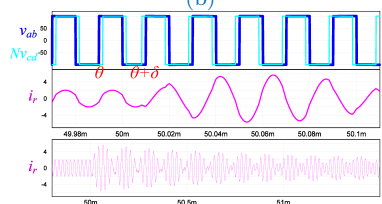
Figure 32: **CTPSM** for (a)  $\delta > 0$  and (b)  $\delta < 0$ .



(a)



(b)



(c)

Figure 33: Simulated transient responses under **CTPSM**. (a) Step-load increase:  $\theta = \pi/6$ ,  $\delta = \pi/6$  and  $\theta + \delta = \pi/3$ . (b) Step-load decrease:  $\theta = \pi/3$ ,  $\delta = -\pi/6$  and  $\theta + \delta = \pi/6$ . (c) Step change of power flow direction:  $\theta = \pi/6$ ,  $\delta = -\pi/3$  and  $\theta + \delta = -\pi/6$ .



# TSM: Increasing Power ( $\delta > 0$ )

★ The transient oscillations occur at the beat frequency:  $f_B = f_s - f_r$ .

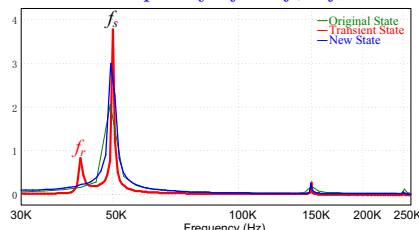


Figure 34: Frequency spectrum of  $i_r$ .

## Boundary Constrain Conditions

Assuming the transient process begins at  $\phi_4^I/\omega_s$  and ends at  $\phi_8^I/\omega_s$ .

$$i_r\left(\frac{\phi_8^I}{\omega_s}\right) = i_r\left(\frac{\phi_{12}^I}{\omega_s}\right) \quad (21)$$

$$v_{Cr}\left(\frac{\phi_8^I}{\omega_s}\right) = v_{Cr}\left(\frac{\phi_{12}^I}{\omega_s}\right) \quad (22)$$

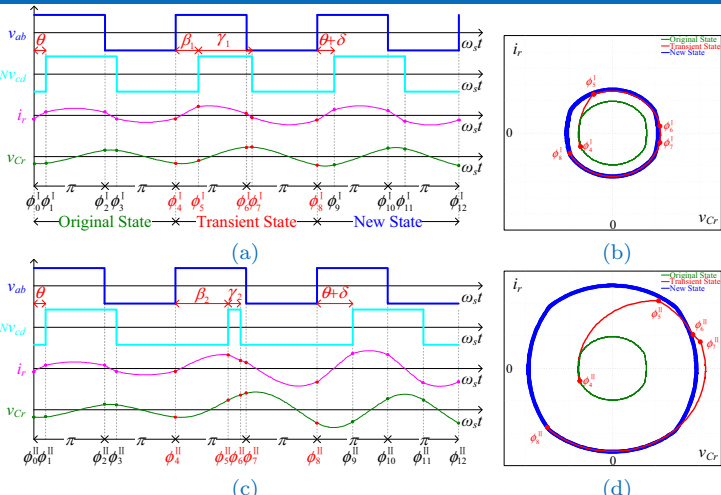


Figure 35: The proposed TSM for  $\delta > 0$ . (a) Mode I, (c) Mode II. 2D state-plane diagrams under TSM ( $\delta > 0$ ). (b) Mode I. (d) Mode II.



# TSM: Decreasing Power ( $\delta < 0$ )

**closed-form solutions for  $\gamma_1 > 0$ :**

$$\beta_1 = \frac{\pi + 2\theta + \delta - \gamma_1}{2} \quad (23)$$

$$\gamma_1 = 2F \cdot \arcsin \left[ \frac{1}{2} \sec \left( \frac{\pi}{2F} \right) \sin \left( \frac{2\pi + \delta}{2F} \right) \right] \quad (24)$$

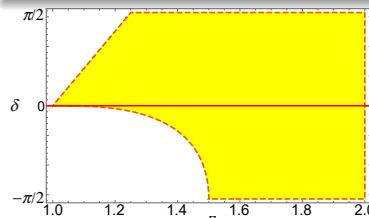


Figure 36: Feasible solution region of (24).

**closed-form solutions for  $\gamma_3 < 0$ :**

$$\beta_3 = \frac{\pi - 2\theta - \delta - \gamma_3}{2} \quad (25)$$

$$\gamma_3 = 2F \cdot \arcsin \left[ \frac{1}{2} \sec \left( \frac{\pi}{2F} \right) \sin \left( \frac{2\pi - \delta}{2F} \right) \right] \quad (26)$$

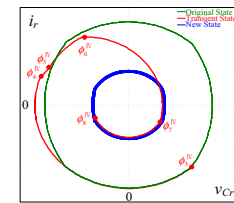
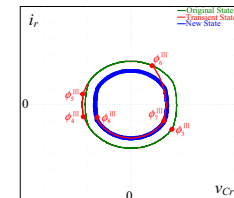
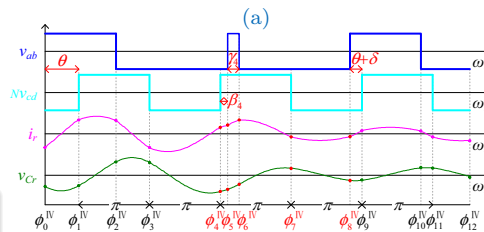
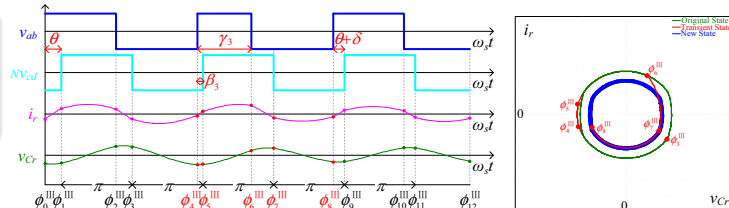


Figure 37: The proposed TSM for  $\delta < 0$ . (a) Mode III. (c) Mode IV. 2D state-plane diagrams under TSM ( $\delta < 0$ ). (b) Mode III. (d) Mode IV.



# Unified Form of TSM

## Simplified Expressions of TSM

The following relationships can be summarized:

$$\textcircled{1} \quad \phi_5^{\text{I}} - \phi_3^{\text{I}} = (\pi - \theta) + \beta_1$$

$$\textcircled{2} \quad \phi_9^{\text{I}} - \phi_7^{\text{I}} = \pi - (\beta_1 + \gamma_1 - \pi) + (\theta + \delta)$$

$$\textcircled{3} \quad \phi_5^{\text{II}} - \phi_3^{\text{II}} = (\pi - \theta) + \beta_2$$

$$\textcircled{4} \quad \phi_9^{\text{II}} - \phi_6^{\text{II}} = (\pi - \beta_2 - \gamma_2) + \pi + (\theta + \delta)$$

$$\textcircled{5} \quad \phi_4^{\text{III}} - \phi_2^{\text{III}} = \theta + (\pi - \beta_3)$$

$$\textcircled{6} \quad \phi_8^{\text{III}} - \phi_6^{\text{III}} = (\pi - (\gamma_3 - \beta_3)) + (\pi - (\theta + \delta))$$

$$\textcircled{7} \quad \phi_5^{\text{IV}} - \phi_2^{\text{IV}} = \theta + \pi + \beta_4$$

$$\textcircled{8} \quad \phi_8^{\text{IV}} - \phi_6^{\text{IV}} = (\pi - \beta_4 - \gamma_4) + (\pi - (\theta + \delta))$$

By combining the above relationships with (23) and (25),  $\beta_1$ ,  $\beta_2$ ,  $\beta_3$ , and  $\beta_4$  can be eliminated, thus resulting in

$$\begin{aligned} \phi_5^{\text{I}} - \phi_3^{\text{I}} &= \phi_9^{\text{I}} - \phi_7^{\text{I}} = \phi_5^{\text{II}} - \phi_3^{\text{II}} = \phi_9^{\text{II}} - \phi_6^{\text{II}} \\ &= \phi_4^{\text{III}} - \phi_2^{\text{III}} = \phi_8^{\text{III}} - \phi_6^{\text{III}} = \phi_5^{\text{IV}} - \phi_2^{\text{IV}} = \phi_8^{\text{IV}} - \phi_6^{\text{IV}} \\ &= (3\pi - \gamma + |\delta|)/2. \end{aligned} \quad (27)$$

😊 The transient pulse width  $\gamma$  of the modulated square-wave voltage ( $v_{ab}$  for  $\delta < 0$  and  $v_{cd}$  for  $\delta > 0$ ) defined by (24) and (26) can be unified as:

$$\gamma = 2F \arcsin \left[ \frac{1}{2} \sec \left( \frac{\pi}{2F} \right) \sin \left( \frac{2\pi + |\delta|}{2F} \right) \right] \quad (28)$$

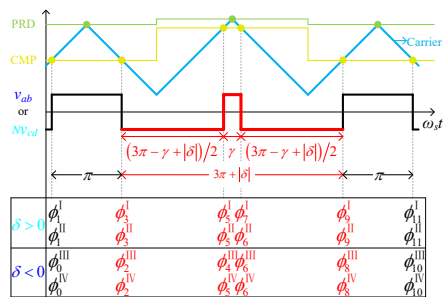
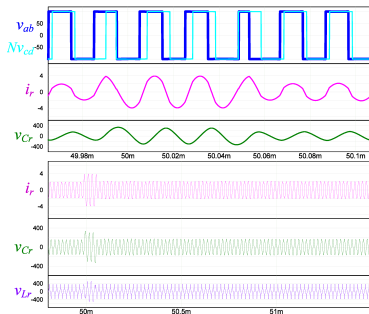


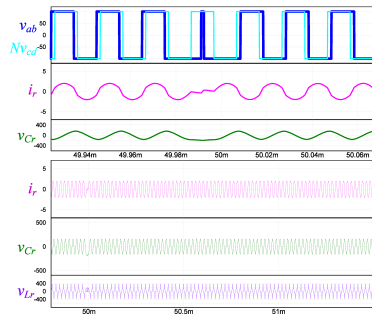
Figure 38: Unified form of TSM.



# Simulated Open-Loop Results Under TSM



(a)



(b)

**Figure 39:** Simulated open-loop transient responses under TSM. (a) The phase-shift angle is changed from  $\pi/6$  to  $\pi/3$  and back to  $\pi/6$ . (b) The phase-shift angle is changed from  $\pi/6$  to  $-\pi/6$ .

■ ☺ No transient oscillations in different open-loop conditions.

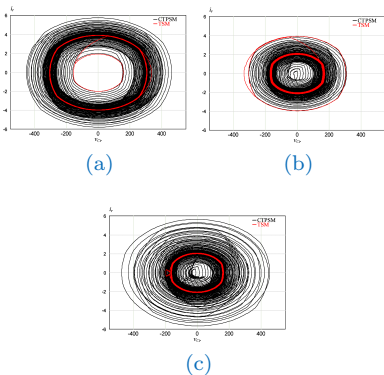


**Figure 40:** Transient open-loop state-plane diagrams of SR-DABC under CTPSM and TSM. (a)  $\theta = \pi/6$ ,  $\delta = \pi/6$  and  $\theta + \delta = \pi/3$ . (b)  $\theta = \pi/3$ ,  $\delta = -\pi/6$  and  $\theta + \delta = \pi/6$ . (c)  $\theta = \pi/6$ ,  $\delta = -\pi/3$  and  $\theta + \delta = -\pi/6$ .



# MPC Design for SPS-Modulated SR-DABC

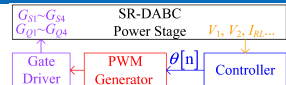
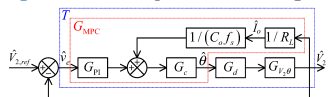


Figure 41: Conceptual block diagram.



(a)

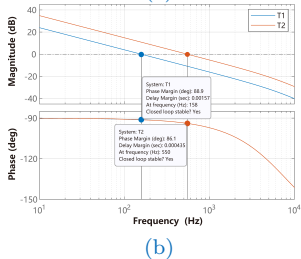


Figure 42: (a) Small-signal block diagram. (b) Bode plot of loop gain  $T(s)$ .

## Key Design Procedures

- ① (29) describes the dynamic behavior of  $V_2$ :

$$C_o \frac{dV_2}{dt} = \bar{i}_2 - I_o = \frac{P}{V_2} - I_o = \frac{8NV_1 \sin \theta}{\pi^2 X_r} - \frac{V_2}{R_L} \quad (29)$$

- ② Discretizing (29) by using forward Euler approximation yields (30),

$$V_2[n+1] = V_2[n] + V_2'[n]T_s = V_2[n] + \frac{8NV_1 \sin \theta}{\pi^2 X_r C_o f_s} - \frac{V_2[n]}{R_L C_o f_s} \quad (30)$$

- ③ The cost function  $J$  is formulated as  $J = [V_{2,ref} - V_2[n+1]]^2$ .

- ④ Minimizing  $J$  ( $\nabla J = 0$ ) gives the optimal phase-shift angle:

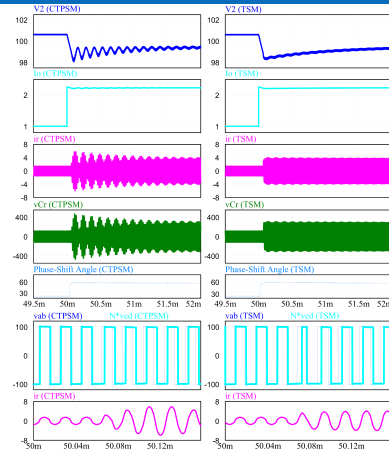
$$\theta[n+1] = \arcsin \left[ \frac{\pi^2 X_r C_o f_s}{8NV_1[n]} \left[ v_e[n] + \frac{I_o[n]}{C_o f_s} \right] \right] \quad (31)$$

- ⑤ A PI compensator is introduced to compensate for unmodeled effects and act as a low-pass filter for attenuating HF noise and ensuring loop stability. The overall transfer function is given by:

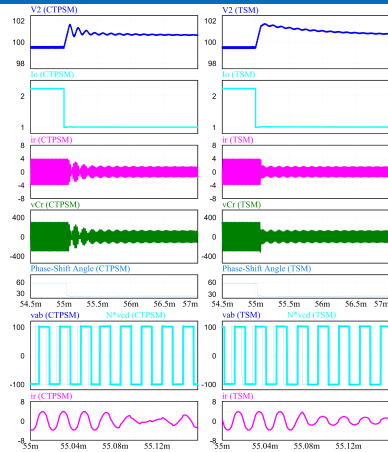
$$G_{MPC}(s) = W \left[ \hat{v}_e[n] \left( K_p + \frac{K_i}{s} \right) + \frac{\hat{I}_{RL}[n]}{C_o f_s} \right] / \sqrt{1 - \left[ \frac{W I_o[n]}{C_o f_s} \right]^2} \quad (32)$$



# Closed-Loop Simulation Results #1



(a)



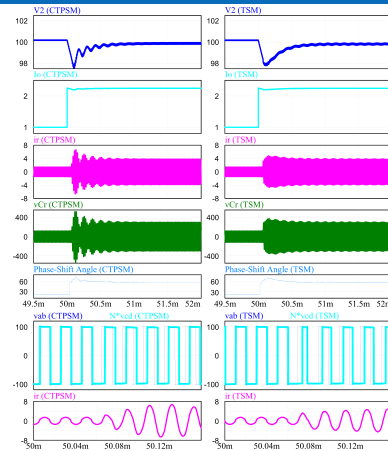
(b)

Figure 43: Simulated transient responses under MPC with  $T_1$  ( $K_p = 0.02$ ,  $K_i = 0.005$ ). (a) Load step-up. (b) Load step-down.

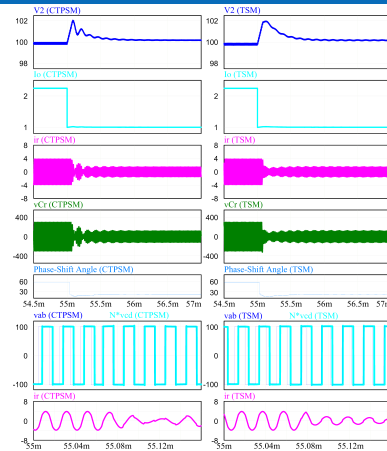
■ The higher the controller gain is, the larger the transient oscillations become.



# Closed-Loop Simulation Results #2



(a)



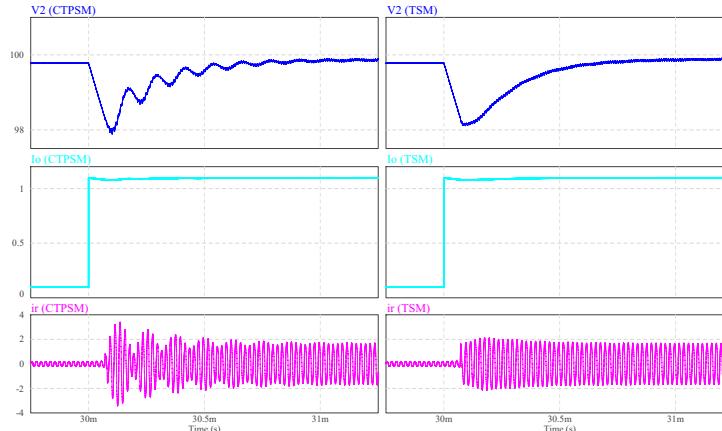
(b)

Figure 44: Simulated transient responses under MPC with  $T_2$  ( $K_p = 0.07$ ,  $K_i = 0.01$ ). (a) Load step-up. (b) Load step-down.

■ ☺ TSM is effective to eliminate the transient oscillations with different control parameters.



# Closed-Loop Simulation Results #3 (modified $R_L$ )



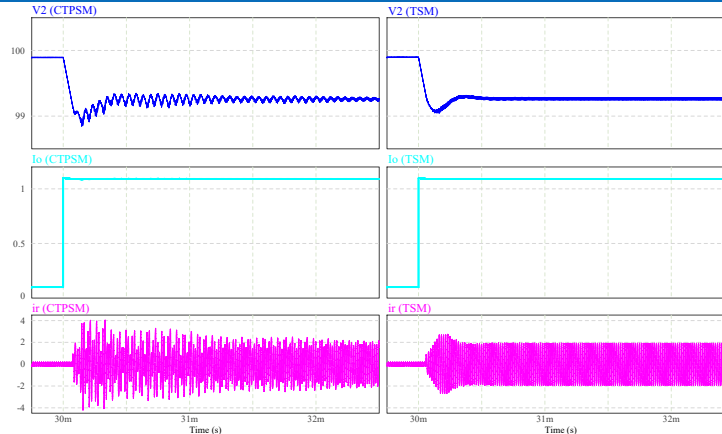
(a)

- ☺ TSM is effective to eliminate the transient oscillations with different amplitudes of load change.



# Closed-Loop Simulation Results #4

(modified  $R_L$ ,  $C_o$ ,  $f_s$ ,  $K_p$ , and  $K_i$ )



(b)

Figure 45: Simulated closed-loop transient responses under MPC with modified parameters. (a)  $C_o = 47\mu F$ ,  $R_L = 1000/90.9\Omega$ ,  $f_s = 50$  kHz,  $K_p = 0.07$ , and  $K_i = 0.01$  (i.e.,  $T_2$ ). (b)  $C_o = 100\mu F$ ,  $R_L = 1000/90.9\Omega$ ,  $f_s = 60$  kHz,  $K_p = 0.3$ , and  $K_i = 0.9$ .

■ ☺ TSM is still effective to eliminate the transient oscillations with different system parameters.



# Experimental Setup of SR-DABC

Table 3: Circuit Parameters of SR-DABC.

Item	Description
Rated Output Power $P_{max}$	250 W
Input Voltage $V_1$	100 V
Output Voltage $V_2$	100 V
Output Capacitance $C_o$	47 $\mu$ F
Load Resistance $R_L$	100/45 $\Omega$
Transformer Turns Ratio $N : 1$	1 : 1
Resonant Inductance $L_r$	321 $\mu$ H
Equivalent series resistance of $L_r$	211 m $\Omega$
Resonant Capacitance $C_r$	45 nF
Resonant Frequency $f_r$	41.8756 kHz
Switching Frequency $f_s$	50 kHz
Dead Time	300 ns
Switches $S_1 \sim S_4$ and $Q_1 \sim Q_4$	UnitedSiC UJC06505K
Drain-Source ON Resistance	45 m $\Omega$
Gate Driver	TI UCC21520
Op Amp for ADC	TI TL082
Voltage Transducer	Two-Resistor Voltage Divider
Current Transducer	LEM LA 55-P
Microprocessor	TI TMS320F28335
Simulation Software	PSIM 12.0.4

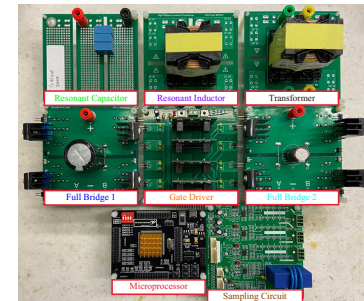


Figure 46: Photograph of the SR-DABC prototype.

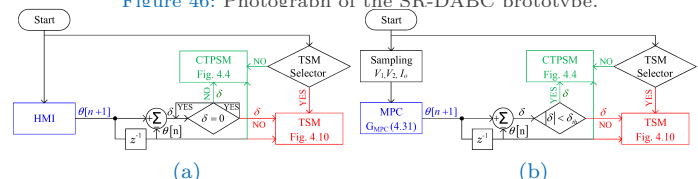
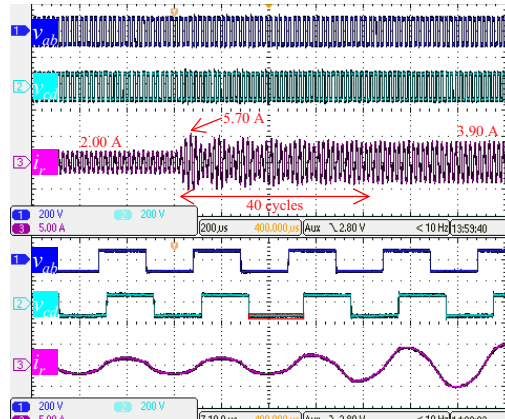


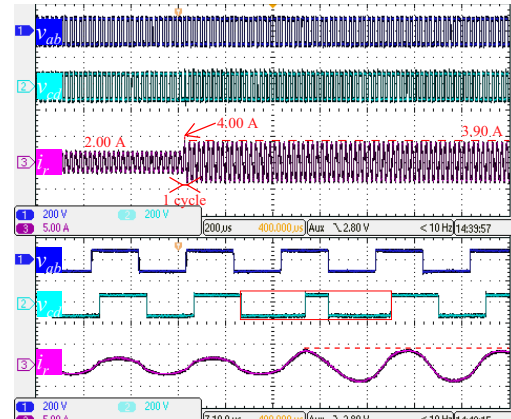
Figure 47: Implementation flowcharts.  
(a) Open-loop configuration. (b) Closed-loop configuration.



# Open-Loop Tests #1 CTPSM v.s. TSM



(a)



(b)

**Figure 48:** Open-loop experimental results when the phase-shift angle is changed from  $\pi/6$  to  $\pi/3$ . (a) Under CTPSM (c.f. simulation results in Fig. 33(a)). (b) Under TSM (c.f. simulation results in Fig. 39(a)).

# Open-Loop Tests #2 CTPSM v.s. TSM

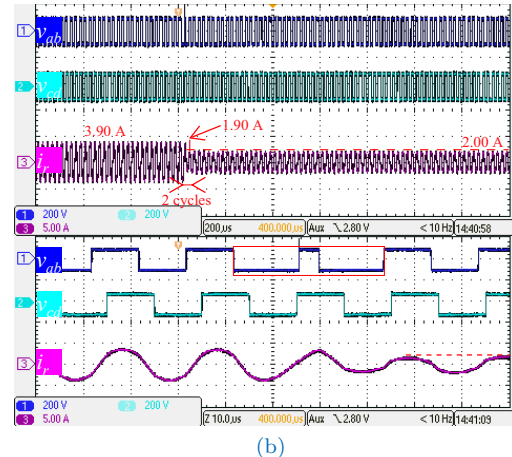
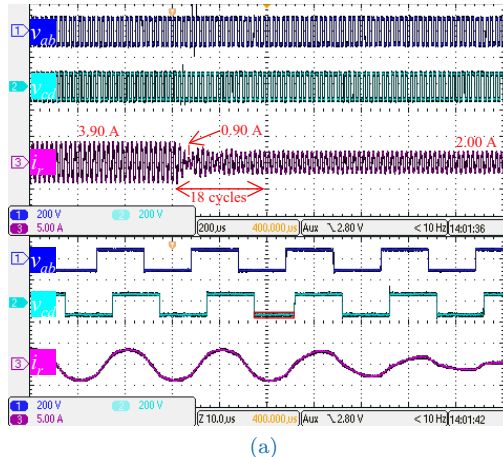
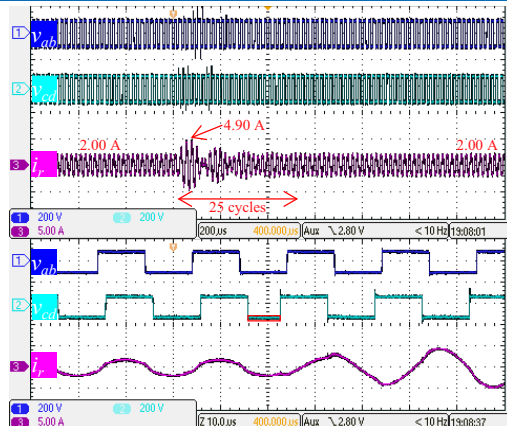


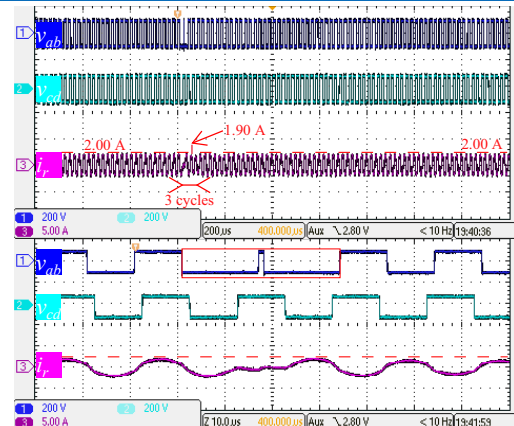
**Figure 49:** Open-loop experimental results when the phase-shift angle is changed from  $\pi/3$  to  $\pi/6$ . (a) Under CTPSM (c.f. simulation results in Fig. 33(b)). (b) Under TSM (c.f. simulation results in Fig. 39(a)).



# Open-Loop Tests #3 CTPSM v.s. TSM



(a)



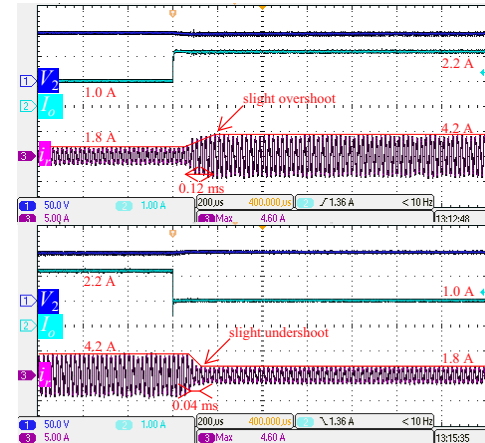
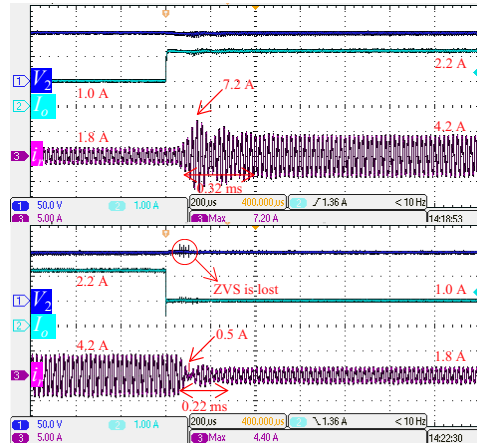
(b)

Figure 50: Open-loop experimental results when the phase-shift angle is changed from  $\pi/6$  to  $-\pi/6$ . (a) Under CTPSM (c.f. simulation results in Fig. 33(c)). (b) Under TSM (c.f. simulation results in Fig. 39(b)).

■ ☺ TSM can eliminate transient oscillations in different open-loop conditions.



# Closed-Loop Tests MPC+CTPSM v.s. MPC+TSM

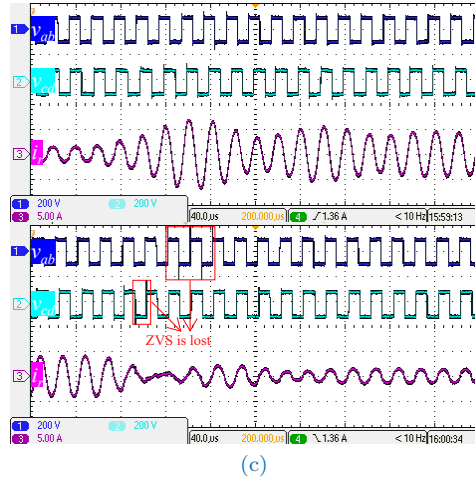


- Smiley face icon: No visible overshoot and undershoot are observed in  $i_r$  during step-load increase and decrease when TSM is applied instead of CTPSM, and TSM can achieve high-quality transient waveforms.

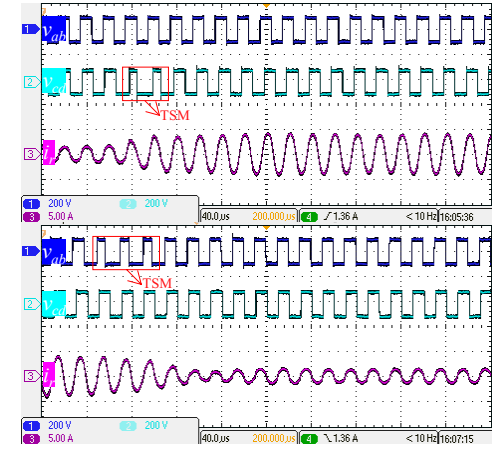


# Closed-Loop Tests MPC+CTPSM v.s. MPC+TSM

(zoomed-in waveforms of  $v_{ab}$ ,  $v_{cd}$ , and  $i_r$ )



(c)

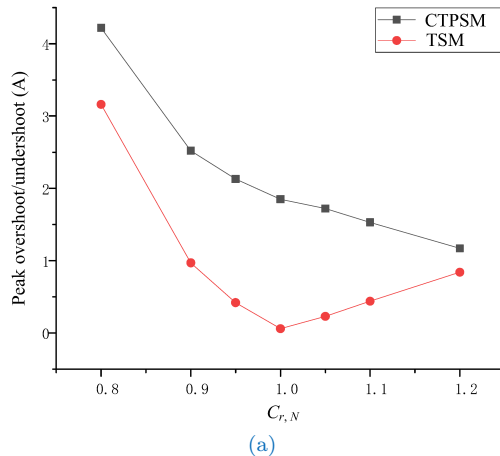


(d)

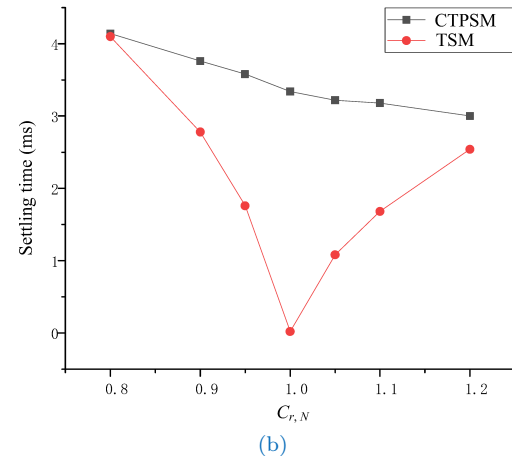
Figure 51: Experimental step-load transient responses under (a) MPC+CTPSM, (b) MPC+TSM. Zoomed-in waveforms of  $v_{ab}$ ,  $v_{cd}$ , and  $i_r$  under (c) MPC+CTPSM, (d) MPC+TSM. ( $T_2$ :  $K_p=0.07$ ,  $K_i=0.01$ )



# Parameter Sensitivity Analysis (PSA) #1



(a)

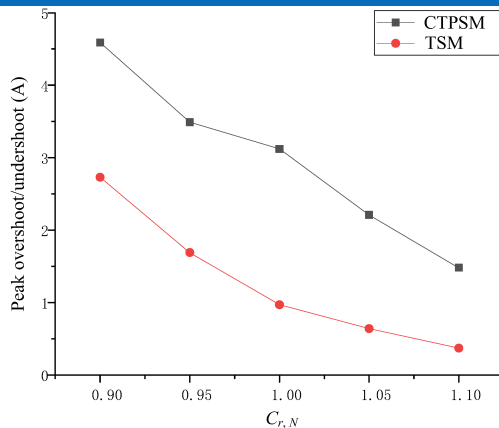


(b)

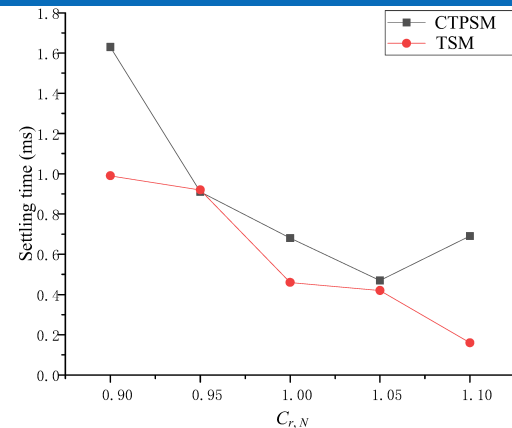
**Figure 52:** Open-loop PSA results for an increase in phase-shift angle from  $\pi/6$  to  $\pi/3$ . (a) Peak overshoot/undershoot. (b) Settling time.



# Parameter Sensitivity Analysis (PSA) #2



(a)



(b)

Figure 53: Closed-loop PSA results for a step-load increase from 1 A to 2.2 A. (a) Peak overshoot/undershoot. (b) Settling time.

■ ☺ TSM is still effective even after taking the effect of parameter variation into consideration.



# Contents

- ▶ Introduction
- ▶ Overview of Existing Modulation and Control Strategies
- ▶ Optimal Transient SPS Modulation for NR-DABC
- ▶ Trajectory-Switching Modulation for SR-DABC
- ▶ Generalized Trajectory-Switching Modulation for DABC
- ▶ Conclusions





# Why is GTSM Required?

## 😢 Some Limitations of the OTPSM Schemes Developed for SR-DABC

- ① MPS gating schemes can improve DABC's efficiency. However, the feasible solution region of TSM is restricted when  $f_s$  approaches  $f_r$ , which makes it inconvenient to use in MPS-modulated SR-DABC. It is also unfeasible to extend the transient modulation methods in [109]-[111] to MPS modulation.
- ② All prior methods cannot eliminate the transient dc offset in transformer's magnetizing current.
- ③ As discussed in Figs. 52 and 53, the performance of both MPCs and the transient modulation methods developed for SR-DABC can be affected by the switching-to-resonant frequency ratio  $F = f_s/f_r$ . When the resonant tank's parameters are not precisely known or deviate significantly from the nominal values, a parameter estimation method is desirable to ensure SR-DABC can adaptively achieve good dynamics.

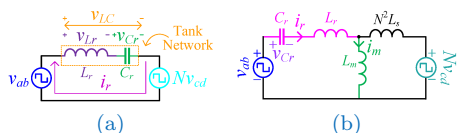


Figure 54: Two equivalent circuits of SR-DABC (a) without magnetizing inductance  $L_m$  and (b) with  $L_m$ .

Table 4: Comparison of transient modulation schemes for SR-DABC.

Desirable properties	GTSM	TSM [140]	Methods in [109]–[111]
Oscillation Suppression	✓	✓	✓
DC-offset Elimination	✓	✗	✗
Generic Method	✓	✗	✗
Analytical Expression	✓	✓	✗
Sensorless Algorithm	✓	✓	✗
Closed-loop Implementation	✓	✓	✗
Wide Feasible Region	✓	✗	Not applicable



# Equivalent Circuit Model of TPS-modulated SR-DABC

$v_{ab}$  and  $v_{cd}$  under any commonly used fixed-frequency phase-shift modulation schemes can be seen as produced by four independent half-bridge square-wave generators (i.e.,  $v_{ao}$ ,  $-v_{bo}$ ,  $v_{co'}$ , and  $-v_{do'}$ ).

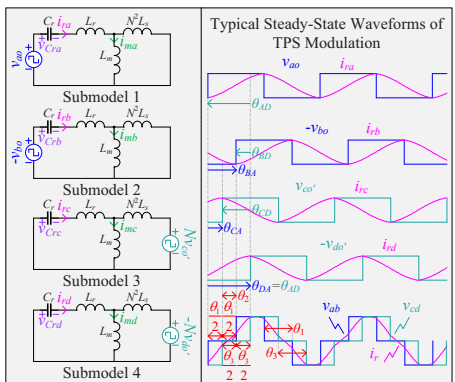


Figure 55: Half-bridge equivalent model.

Table 5: Relationships Between Different Definitions of Phase-Shift Angles.

Reference Signal	Phase-Shift Relationship	Reference Signal	Phase-Shift Relationship
$v_{ao}$	$\theta_{BA} = \theta_1$	$-v_{do'}$	$\theta_{AD} = \theta_2 + 0.5 * (\theta_1 + \theta_3)$
	$\theta_{CA} = \theta_2 + 0.5 * (\theta_1 - \theta_3)$		$\theta_{BD} = \theta_2 + 0.5 * (\theta_3 - \theta_1)$
	$\theta_{DA} = \theta_2 + 0.5 * (\theta_1 + \theta_3)$		$\theta_{CD} = \theta_3$

## Contribution of Each Independent Excitation Source

Using the superposition theorem yields

$$\begin{cases} i_r = i_{ra} + i_{rb} + i_{rc} + i_{rd} \\ i_m = i_{ma} + i_{mb} + i_{mc} + i_{md} \\ v_{Cr} = v_{Cra} + v_{Crb} + v_{Crc} + v_{Crd} \end{cases} \quad (33)$$

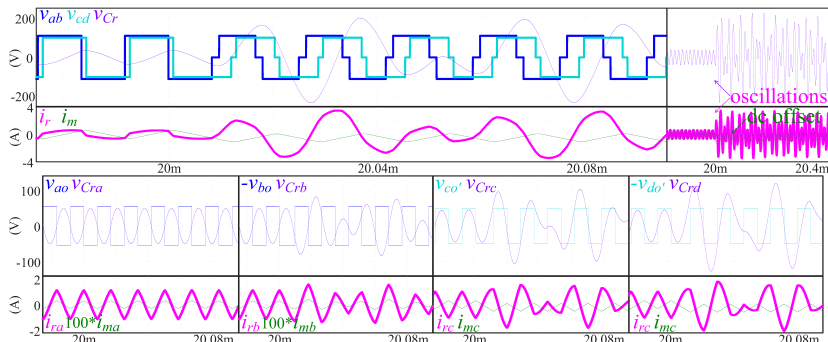
Applying mesh analysis to submodel 2 and submodel 3

$$i_{mb} = \frac{N^2 L_s}{L_m + N^2 L_s} i_{rb} \quad (34)$$

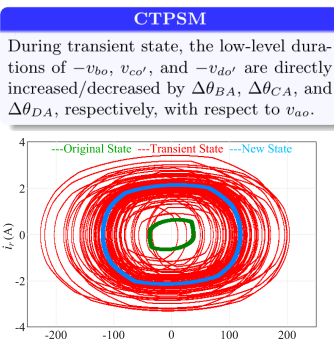
$$i_{mc} = \left( \frac{1}{\omega_s^2 L_m C_r} - \frac{L_r}{L_m} \right) i_{rc} \quad (35)$$

# Open-Loop Simulation Example under CTPSM

from SPS Mode to TPS Mode



(a)



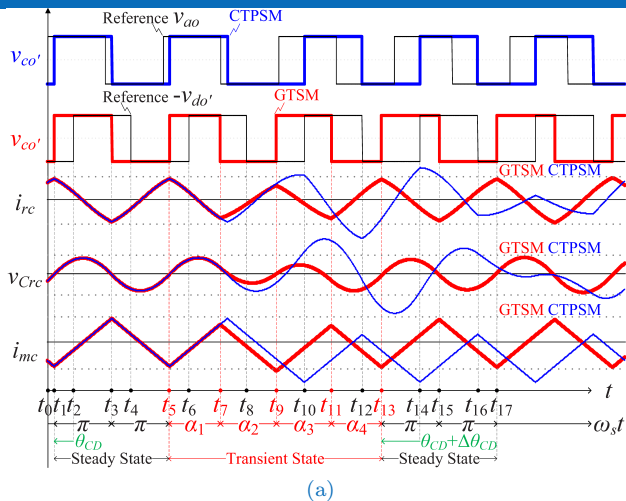
(b)

**Figure 56:** An open-loop simulation example under CTPSM with  $V_1 = 110$  V,  $V_2 = 100$  V,  $f_s = 60$  kHz, and  $F = 1.54$ . In this simulation test, the scenario  $\theta_1 = 0$ ,  $\theta_2 = \pi/9$ ,  $\theta_3 = 0$ ,  $\Delta\theta_1 = \pi/6$ ,  $\Delta\theta_2 = 11\pi/36$ , and  $\Delta\theta_3 = \pi/9$ , i.e., a transition from SPS mode to TPS mode is simulated. (a) Simulated transient waveforms. (b)  $v_{Cr}$ - $i_r$  state-plane diagram under CTPSM.

- 😞 Obvious transient oscillations and dc offset can be observed under CTPSM.

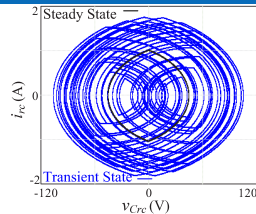


# Design Principles of GTSM

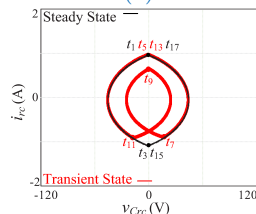


(a)

Figure 57: (a) Theoretical transient waveforms with CTPSM and the proposed GTSM in submodel 3. (b)  $v_{Crc}-i_{rc}$  state-plane diagram under CTPSM. (c)  $v_{Crc}-i_{rc}$  state-plane diagram under GTSM.



(b)



(c)

# Boundary Conditions

for Realizing DC-Offset-Free Transient Response



## Elimination of Transient DC Offset

According to (34), any operation in  $i_{mc}$  and/or  $i_{md}$  may result in large transient dc offsets. It is suggested that  $-v_{do'}$  is fixed and used as the reference signal.

The constraint for achieving dynamic volt-second balance during transient state

$$Nv_{co'}\alpha_1 - Nv_{co'}\alpha_2 + Nv_{co'}\alpha_3 - Nv_{co'}\alpha_4 = 0 \Rightarrow \alpha_1 - \alpha_2 + \alpha_3 - \alpha_4 = 0 \quad (36)$$

Phase-shift constraint (to ensure that the transient state ends no later than  $t_{13}$ )

$$\omega_s(t_{13} - t_5) = \alpha_1 + \alpha_2 + \alpha_3 + \alpha_4 = 4\pi - \Delta\theta_{CD} \quad (37)$$

Combining (36) and (37) leads to

$$\alpha_1 + \alpha_3 = \alpha_2 + \alpha_4 = 2\pi - 0.5\Delta\theta_{CD} \quad (38)$$

To minimize the adverse effects caused by transient dc offset, it is important to minimize the time-averaged value of  $i_{mc}$  (i.e.,  $\bar{i}_{mc}$ ) over the transient state.

$$\bar{i}_{mc} = \frac{1}{t_{13} - t_5} \int_{t_5}^{t_{13}} i_{mc} dt = \frac{NV_2}{2L_m} \left( -\frac{T_s}{4} + \frac{2\pi - 0.5\Delta\theta_{CD}}{2} - \frac{\alpha_2\alpha_3}{2\pi - 0.5\Delta\theta_{CD}} \right) \quad (39)$$

For a given  $\Delta\theta_{CD}$ ,  $\bar{i}_{mc}$  reaches its minimum value only when (40) holds

$$\alpha_2 = \alpha_3 = \max(\alpha_2) = \max(\alpha_3) \quad (40)$$

# Boundary Conditions

for Realizing Oscillation-Free Transient Response



## Elimination of Transient Oscillations

$i_{rc}$  and  $v_{Crc}$  can be expressed by (41) and (42), respectively,

$$i_{rc}(t) = i_{rc}(t_i) \cos(\omega_r(t - t_i)) + ((-Nv_{co'}) - v_{Crc}(t_i)) \sin(\omega_r(t - t_i))/Z_r \quad (41)$$

$$v_{Crc}(t) = v_{Crc}(t_i) \cos(\omega_r(t - t_i)) + Z_r i_{rc}(t_i) \sin(\omega_r(t - t_i)) + (-Nv_{co'})(1 - \cos(\omega_r(t - t_i))) \quad (42)$$

The sufficient and necessary condition for effectively suppressing the transient oscillations in  $i_{rc}$  and  $v_{Crc}$  is that their new steady-state values at  $t_{13}$  should be equal to their initial steady-state values at  $t_5$ .

$$\begin{cases} i_{rc}(t_{13}) = i_{rc}(t_5) \\ v_{Crc}(t_{13}) = v_{Crc}(t_5). \end{cases} \quad (43)$$

A 4-DOF general solution for the suppression of transient oscillations in  $i_{rc}$  and  $v_{Crc}$ :

$$2 \cos\left[\frac{\alpha_3 + \alpha_4 - \alpha_1}{2F}\right] \sin\left[\frac{\alpha_2}{2F}\right] = \sin\left[\frac{2\pi - 0.5\Delta\theta_{CD} - \alpha_4}{F}\right] \quad (44)$$

## 😊 GTSM — Optimal 4-DOF Transient Phase-Shift Modulation

To achieve oscillation-free and dc-offset-free dynamics should simultaneously satisfy (38) and (44). Through a careful analysis, only one particular solution set, i.e., the proposed GTSM (45) is available.

$$\begin{cases} \alpha_1 = \alpha_4 = 2\pi - 0.5\Delta\theta_{CD} - \alpha_2 \\ \alpha_2 = \alpha_3 = F \arccos\left[\left(1 + \cos\left[\frac{3\pi - \Delta\theta_{CD}}{2F}\right]\right) \sec\left[\frac{\pi}{2F}\right]\right]/2 \end{cases} \quad (45)$$



# Performance Evaluation of GTSM

## Comparisons of Different OTPSM Strategies for SR-DABC

- There are no analytical solutions for the transient modulation strategies in [109]-[111], which makes them unsuitable in closed-loop applications.
- The proposed 3-DOF TSM strategy is a particular solution of (44), and there exists no feasible 2-DOF modulation schemes for (44).
- GTSM can be utilized over a wide range of  $f_s$  (i.e., it produces feasible solutions for small  $F$ ), and its feasible region is much larger than that of TSM. Hence, GTSM can be applied in any submodels without changing the reference signal. This makes GTSM easy to use in MPS schemes.
- Until now, the proposed GTSM strategy is the only unified approach capable of simultaneously eliminating transient oscillations and dc offsets in MPS-modulated DABC.
- A transient modulation scheme developed for SR-DABC may be applicable to NR-DABC (e.g., GTSM), but the inverse is not true.

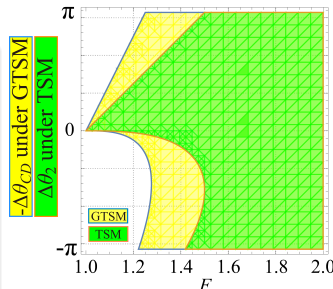


Figure 58: Feasible regions of GTSM and TSM.

😊 When  $F \rightarrow \infty$ , conventional NR-DABC can be regarded as a special case of SR-DABC with infinite  $C_r$ , and (45) can be simplified to (46) for using in NR-DABC.

$$\begin{cases} \alpha_1 = \alpha_4 = \pi - 0.5\Delta\theta_{CD} \\ \alpha_2 = \alpha_3 = \pi \end{cases} \quad (46)$$



# Open-Loop Simulation Example under TSM

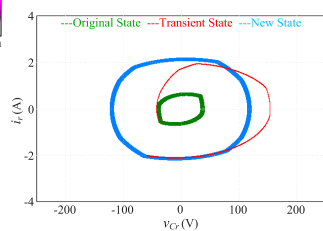
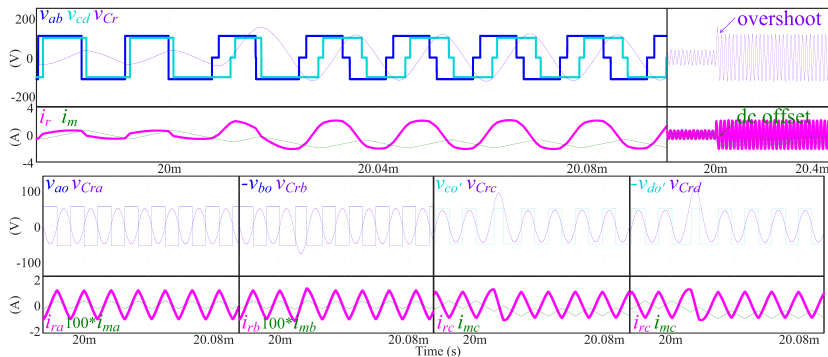
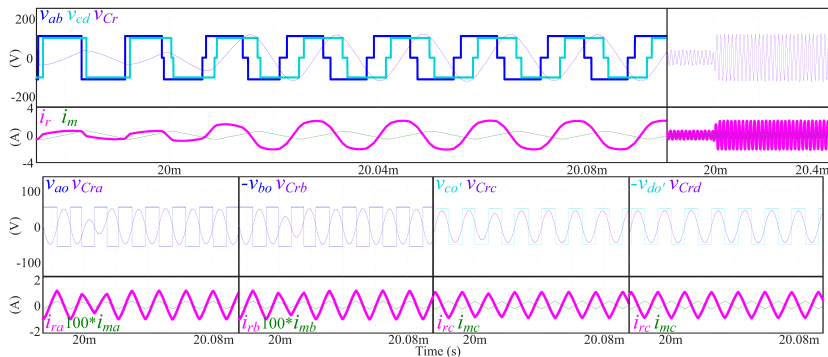


**Figure 59:** The open-loop simulation examples from SPS mode to TPS mode under TSM with  $V_1 = 110$  V,  $V_2 = 100$  V,  $f_s = 60$  kHz, and  $F = 1.54$ . (a) Simulated transient waveforms under TSM. (b)  $v_{Cr}$ - $i_r$  state-plane diagrams under TSM.

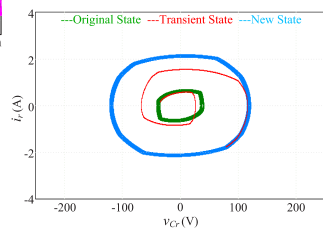
- 😞 Although TSM is able to suppress transient oscillations, it still leads to excessive transient dc offsets in  $i_m$  and some overshoots in  $v_{Cr}$ .
- 😞 Note that TSM is only suitable for use with MPS gating schemes when  $F$  is large.



# Open-Loop Simulation Example under GTSM



(a)



(b)

**Figure 60:** The open-loop simulation examples from SPS mode to TPS mode under GTSM with  $V_1 = 110$  V,  $V_2 = 100$  V,  $f_s = 60$  kHz, and  $F = 1.54$ . (a) Simulated transient waveforms under GTSM. (b)  $v_{Cr}$ - $i_r$  state-plane diagrams under GTSM.

- ☺ GTSM can achieve a transient performance without overshoot, transient dc offset and oscillations.
- ☺ GTSM produces lower energy trajectories of  $i_r$  and  $v_{Cr}$  and represents a significant improvement over TSM, even when F is large.



# Minimum-RMS-Current Operation for SR-DABC

## Minimizing $i_{r\text{-RMS}}$

To maintain a high efficiency during steady state,  $i_{r\text{-RMS}}$  should be minimized for reducing conduction loss.

$$i_{r\text{-RMS}} = \sqrt{\frac{1}{T_s} \int_0^{T_s} i_r^2 dt} = \frac{2\sqrt{2}V_1}{\pi X_r} \sqrt{\cos^2\left[\frac{\theta_1}{2}\right] + M^2 \cos^2\left[\frac{\theta_3}{2}\right] - 2M \cos\left[\frac{\theta_1}{2}\right] \cos\left[\frac{\theta_3}{2}\right] \cos[\theta_2]} \quad (47)$$

$$P_o = \frac{1}{T_s} \int_0^{T_s} v_{ab} \cdot i_r dt = \frac{8NV_1V_2}{\pi^2 X_r} \sin[\theta_2] \cos\left[\frac{\theta_1}{2}\right] \cos\left[\frac{\theta_3}{2}\right] \quad (48)$$

The optimal steady-state phase-shift angles can be obtained by solving the constrained minimization problem:

$$\underset{\theta_1, \theta_2, \theta_3}{\text{minimize}} \quad i_{r\text{-RMS}}(\theta_1, \theta_2, \theta_3), \quad \text{subject to} \quad P_o(\theta_1, \theta_2, \theta_3) = P_{o-d} \quad \& \quad |P_{o-d}| \leq P_{o\text{-max}} \quad (49)$$

The optimal solution sets can be solved by using the method of Lagrange multipliers:

- Case 1 ( $M > 1$  and  $|P_{o-n}| \leq \sqrt{1 - 1/(M^2)}$ ):

$$\theta_1 = 0, \theta_2 = \arctan[P_{o-n} \cdot M], \theta_3 = 2 \arccos\left[\sqrt{1/(M^2) + P_{o-n}^2}\right] \quad (50)$$

- Case 2 ( $M < 1$  and  $|P_{o-n}| \leq \sqrt{1 - M^2}$ ):

$$\theta_1 = 2 \arccos\left[\sqrt{M^2 + P_{o-n}^2}\right], \theta_2 = \arctan[P_{o-n}/M], \theta_3 = 0 \quad (51)$$

- Case 3 (other operating regions):

$$\theta_1 = 0, \theta_2 = \arcsin[P_{o-n}], \theta_3 = 0 \quad (52)$$



# MPC Design for MPS-Modulated SR-DABC

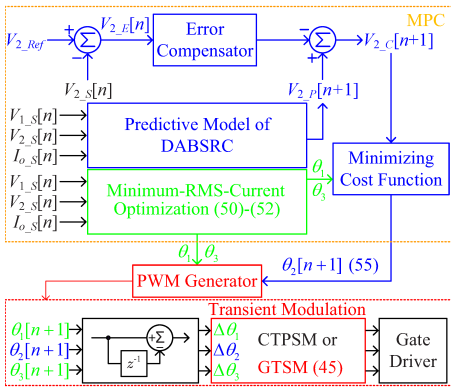


Figure 61: Block diagram of MPC with minimum-RMS-current optimization.

## Control Scheme for MPS-Modulated SR-DABC

The dynamics of  $V_2$  can be obtained as

$$C_o \frac{dV_2}{dt} = \frac{P_o}{V_2} - I_o = \frac{8NV_1}{\pi^2 X_r} \sin[\theta_2] \cos\left[\frac{\theta_1}{2}\right] \cos\left[\frac{\theta_3}{2}\right] - I_o \quad (53)$$

Discretizing (53) using the forward Euler method

$$V_{2\_P}[n + 1] = V_{2\_S}[n] + \frac{dV_{2\_S}[n]}{dt} T_s \quad (54)$$

Minimizing  $\mathcal{J} = (V_{2\_Ref} - V_{2\_C}[n + 1])^2$ , i.e.,  $\nabla \mathcal{J} = 0$ , yields the predicted optimal outer phase-shift angle

$$\begin{aligned} \theta_2[n + 1] = \arcsin & \left[ \frac{\pi^2 X_r C_o f_s}{8NV_{1\_S}[n] \cos \frac{\theta_1}{2} \cos \frac{\theta_3}{2}} \left[ \frac{I_{o\_S}[n]}{C_o f_s} \right. \right. \\ & \left. \left. + K_p^* V_{2\_E}[n] + K_i \sum_{\tau=0}^n V_{2\_E}[\tau] \right] \right] \end{aligned} \quad (55)$$

When implementing the control loop, the outer phase-shift angle  $\theta_2$  is calculated from (55), while the inner phase-shift angles  $\theta_1$  and  $\theta_3$  are directly determined using (50)-(52).



# Simulated Closed-Loop Results

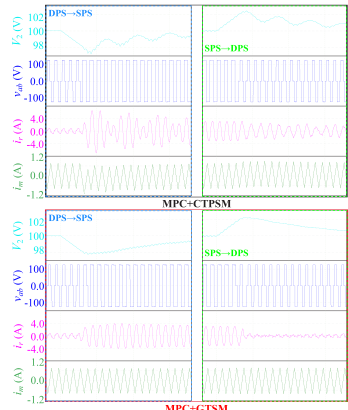
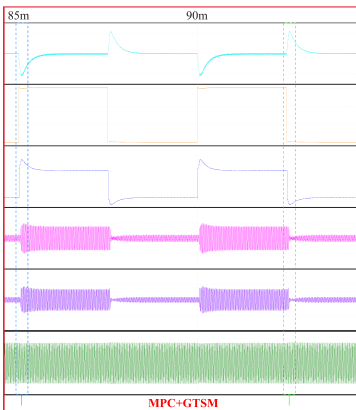
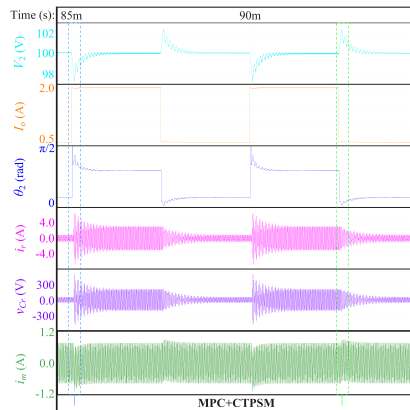


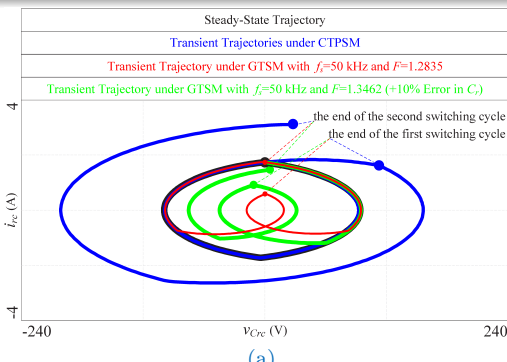
Figure 62: Simulated closed-loop transient waveforms under 200-Hz 0.5-to-2 A pulsed-power loads.  $V_1 = 125$  V,  $V_2 = 100$  V,  $f_s = 50$  kHz,  $F = 1.2835$ ,  $K_p^* = 0.08$ , and  $K_i = 0.00008$ .

■ ☺ It can be seen that the overshoots and undershoots in  $i_r$ ,  $v_{Cr}$ , and  $i_m$  under MPC+CTPSM are significantly larger than those under MPC+GTSM.

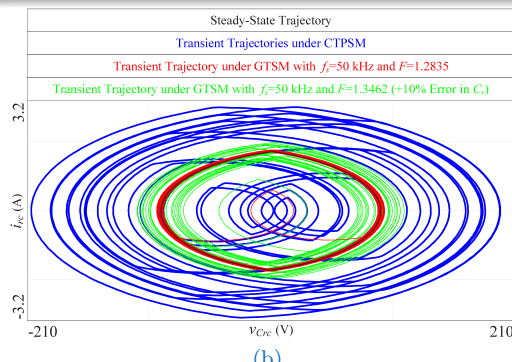


# When $f_r$ Deviates from Its Nominal Value

😢 Due to aging effects, environmental conditions (e.g., temperature and humidity), manufacturing tolerances, etc., the actual values of  $C_r$  and  $L_r$  may deviate from their nominal values. From (45) and (55), the algorithms of both GTSM and MPC are related to  $X_r = \omega_s L_r - 1/(\omega_s C_r)$  and  $F = f_s/f_r = 2\pi f_s \sqrt{L_r C_r}$ , respectively.



(a)



(b)

**Figure 63:** Simulated transient  $v_{Crc}$ - $i_{rc}$  state-plane diagrams in submodel 3 under open-loop conditions, where  $\Delta\theta_3 = \pi/3$  (i.e.,  $\Delta\theta_{CD} = \pi/3$ ),  $f_s = 50$  kHz, and  $F = 1.2835$  (nominal value) or  $F = 1.3462$  (+10% error in  $C_r$ ). (a) Transient  $v_{Crc}$ - $i_{rc}$  state-plane diagrams of the first two switching cycles. (b) Transient  $v_{Crc}$ - $i_{rc}$  state-plane diagrams of 25 switching cycles.



# Automatic Resonant-Frequency Tracking Technique

## A Simple Perturb and Observe (P&O) Method

With large deviations in  $X_r$  and  $F$ , the performances of both PWM generator and controller can be affected. According to (48), the estimation of  $X_r$  under TPS modulation is given by

$$X_r = \omega_s L_r - 1/(\omega_s C_r) = \frac{8NV_1}{\pi^2 I_o} \sin[\theta_2] \cos\left[\frac{\theta_1}{2}\right] \cos\left[\frac{\theta_3}{2}\right] \quad (56)$$

As  $X_r$  changes with  $f_s$  (or  $\omega_s$ ) only,  $f_s$  must be perturbed to produce different values of  $X_r$ .

In theory, for a given switching frequency  $f_{s\_i}$ , its corresponding impedance  $X_{r\_i}$  is given by

$$X_{r\_i} = \sqrt{L_r/C_r} (F_i - 1/F_i) = Z_r (F_i - 1/F_i) \quad (57)$$

Define the nominal impedance  $X_{r\_n}$  at the nominal switching frequency  $f_{s\_n}$  as

$$X_{r\_n} = \sqrt{L_r/C_r} (F_n - 1/F_n) = Z_r (F_n - 1/F_n) \quad (58)$$

Combining (57) and (58), the estimated  $f_r$  and  $F$  can be obtained from (59) and (60).

$$f_{r\_e} = \sqrt{\frac{X_{r\_ie} f_{s\_i} f_{s\_n}^2 - X_{r\_ne} f_{s\_i}^2 f_{s\_n}}{X_{r\_ie} f_{s\_i} - X_{r\_ne} f_{s\_n}}} \quad (59)$$

$$F_{n\_e} = \sqrt{\frac{f_{s\_n} (X_{r\_ie} f_{s\_i} - X_{r\_ne} f_{s\_n})}{f_{s\_i} (X_{r\_ie} f_{s\_n} - X_{r\_ne} f_{s\_i})}} \quad (60)$$



# Experimental Setup of SR-DABC

Table 6: Circuit Parameters of SR-DABC.

Symbol	Parameter Description	Value or Part Type
$V_1$	Input Voltage	110-125 V
$V_2$	Output Voltage	100 V
$C_o$	Output Capacitance	47 $\mu$ F
$R_L$	Load Resistance	50/200 $\Omega$
$N : 1$	Transformer's Turns Ratio	1 : 1
$L_m$	Magnetizing Inductance	650 $\mu$ H
$L_r$	Resonant Inductance	321 $\mu$ H
$L_s$	Secondary Inductance	1.70 $\mu$ H
$C_r$	Resonant Capacitance	52 nF
$f_s$	Switching Frequency	50-60 kHz
$f_r$	Resonant Frequency	38.96 kHz
$S_x \sim Q_x$	Power Switches	UnitedSiC UJC06505K
-	Dead Time	250 ns
-	Gate Driver	TI UCC21520
-	Current Transducer	LEM LA 55-P
-	Voltage Transducer	Resistive Divider
-	Microprocessor	TI TMS320F28335
-	DAC Module	Microchip MCP4921
-	Simulation Platform	Powersim PSIM

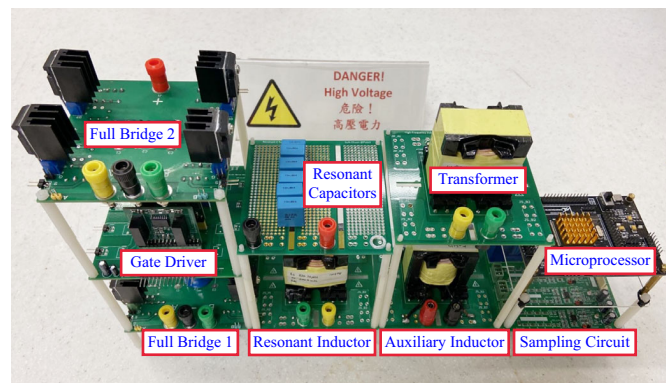


Figure 64: Photograph of laboratory prototype of SR-DABC.



# Open-Loop Tests Under CTPSM v.s. GTSM

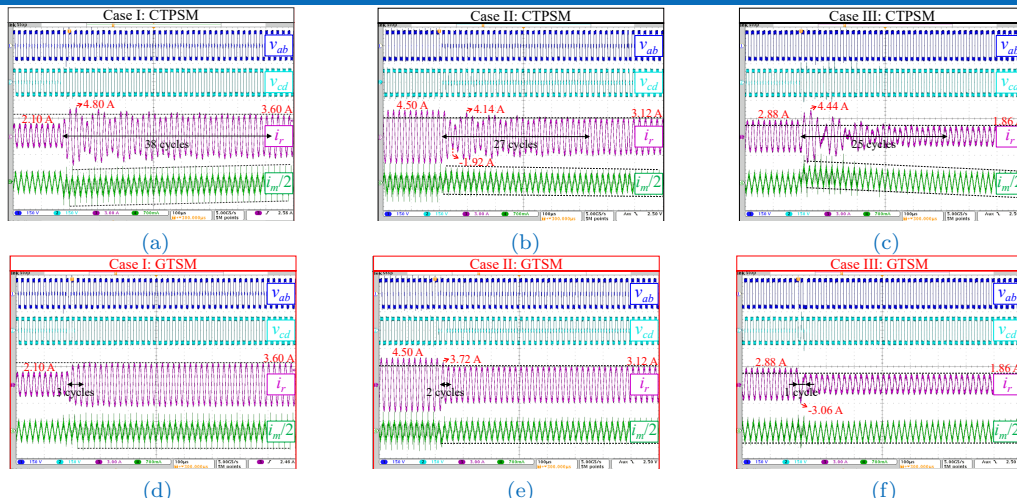
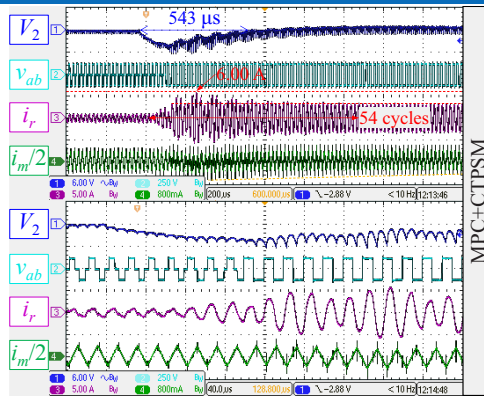


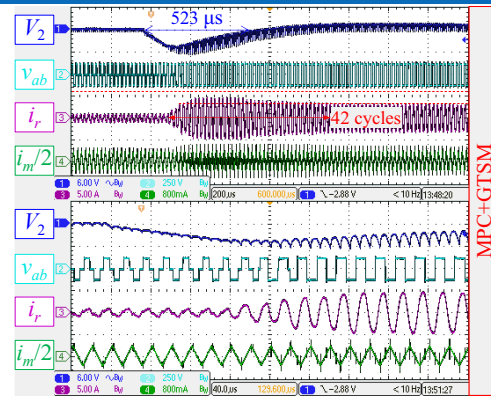
Figure 65: Experimental open-loop transient waveforms with  $V_1 = 110$  V,  $V_2 = 100$  V,  $f_s = 50$  kHz, and  $F = 1.2835$ . (a) and (d) Case I: Increasing power. (b) and (e) Case II: Decreasing power. (c) and (f) Case III: Reversing power flow direction.



# Closed-Loop Tests #1 (a) MPC+CTPSM (b) MPC+GTSM



(a)



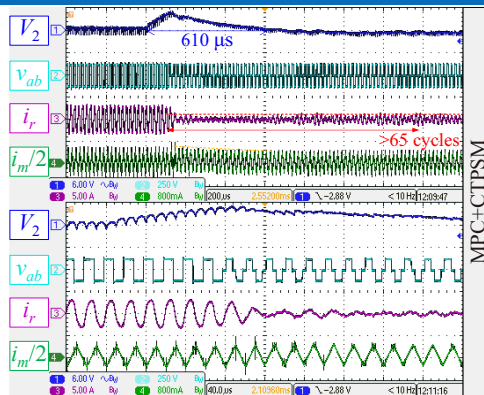
(b)

**Figure 66:** Experimental closed-loop results for a step-up load change from 0.5-2 A with  $\{K_p^* = 0.055, K_i = 0.0015\}$  under (a) MPC+CTPSM and (b) MPC+GTSM.  $V_1 = 125$  V,  $V_2 = 100$  V,  $f_s = 50$  kHz,  $F = 1.2835$ , and  $X_r = 39.6317$ .

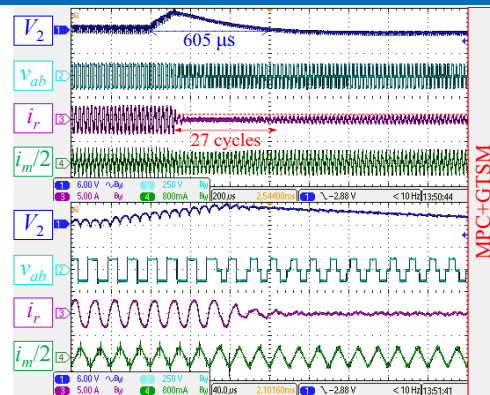
- ☺ The waveforms under MPC+GTSM can approach their new steady-state values rapidly without undergoing any transient oscillations and dc offsets.



# Closed-Loop Tests #2 (a) MPC+CTPSM (b) MPC+GTSM



(a)



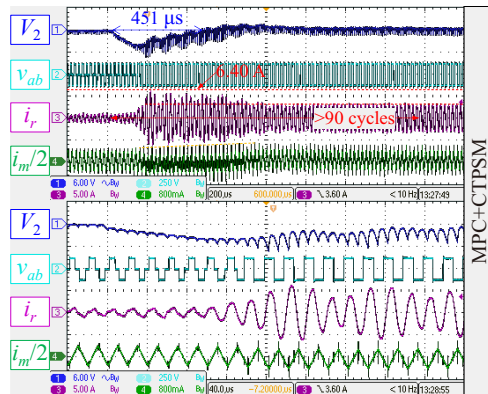
(b)

**Figure 67:** Experimental closed-loop results for a step-down load change from 2-0.5 A with  $\{K_p^* = 0.055, K_i = 0.0015\}$  under (a) MPC+CTPSM and (b) MPC+GTSM.  $V_1 = 125$  V,  $V_2 = 100$  V,  $f_s = 50$  kHz,  $F = 1.2835$ , and  $X_r = 39.6317$ .

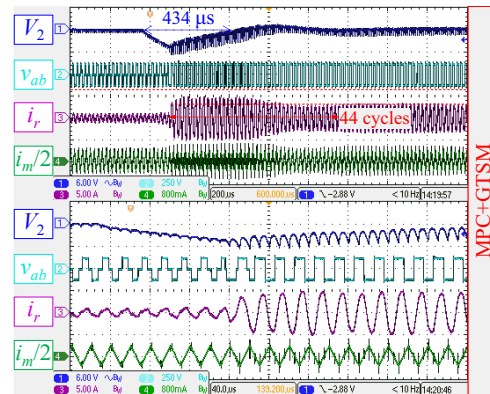
- ☺ The output voltage quality is much improved under MPC+GTSM and does not suffer from any transient oscillations.



# Closed-Loop Tests #3 (a) MPC+CTPSM (b) MPC+GTSM



(a)



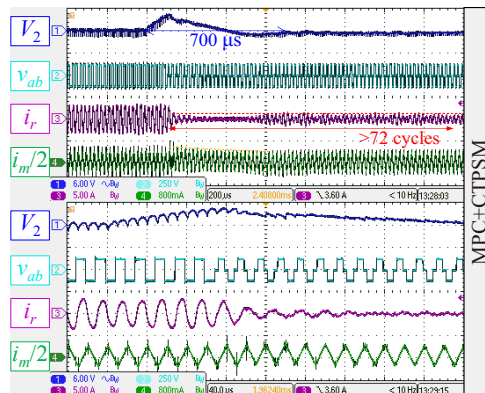
(b)

Figure 68: Experimental closed-loop results for a step-up load change from 0.5 to 2 A with  $\{K_p^* = 0.15, K_i = 0.004\}$  under (a) MPC+CTPSM and (b) MPC+GTSM.  $V_1 = 125$  V,  $V_2 = 100$  V,  $f_s = 50$  kHz,  $F = 1.2835$ , and  $X_r = 39.6317$ .

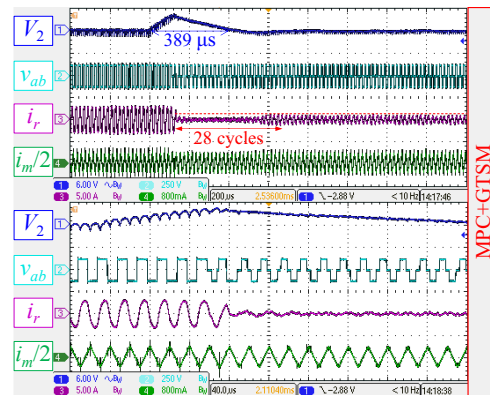
■ 😊 MPC+GTSM leads to shorter recovery time in  $V_2$  and shorter settling times in  $i_r$  and  $i_m$ .



# Closed-Loop Tests #4 (a) MPC+CTPSM (b) MPC+GTSM



(a)



(b)

Figure 69: Experimental closed-loop results for a step-down load change from 2 to 0.5 A with  $\{K_p^*=0.15, K_i=0.004\}$  under (a) MPC+CTPSM and (b) MPC+GTSM.  $V_1=125$  V,  $V_2=100$  V,  $f_s=50$  kHz,  $F=1.2835$ , and  $X_r=39.6317$ .



# Parameter Sensitivity Tests #1 Open-Loop Conditions

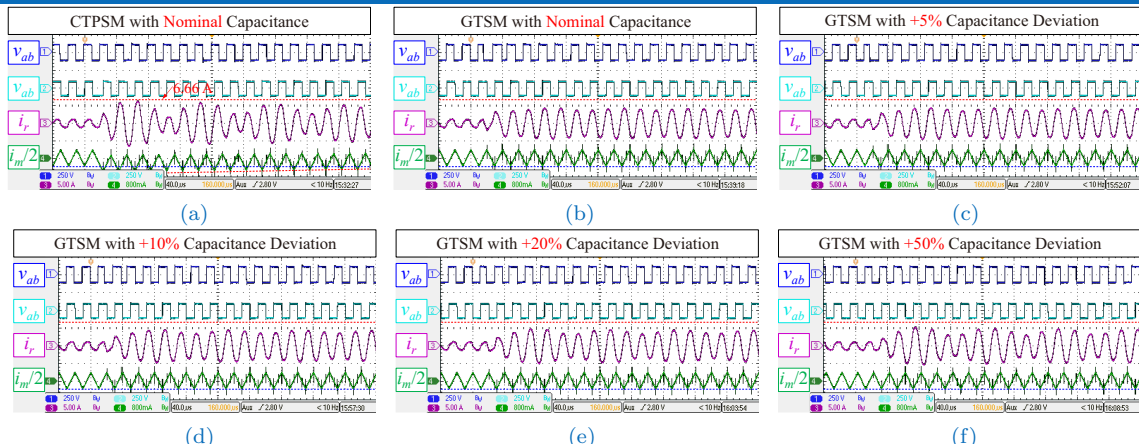


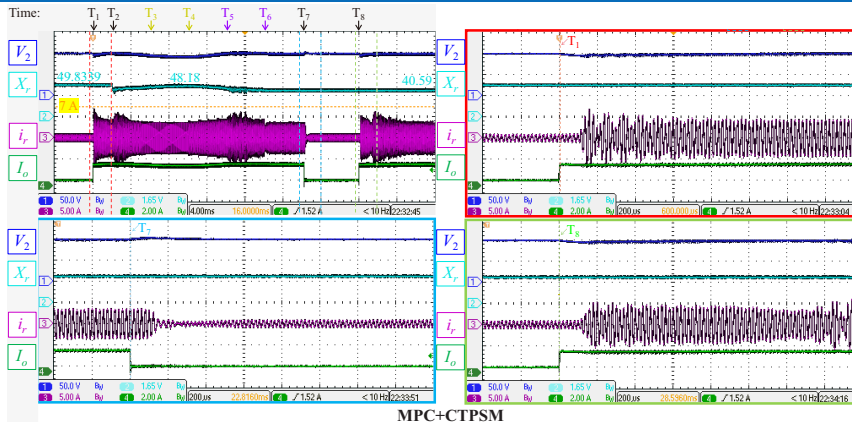
Figure 70: Experimental open-loop transient waveforms under CTPSM and GTSM while considering different capacitance errors.  $V_1 = 110$  V,  $V_2 = 100$  V,  $f_s = 50$  kHz,  $\theta_1 = \Delta\theta_1 = 0$ ,  $\theta_3 = \Delta\theta_3 = 0$ ,  $\theta_2 = \pi/9$ , and  $\Delta\theta_2 = 4\pi/9$ .

Even there exists 50% capacitance deviation, GTSM performs better than CTPSM  
(smaller transient oscillations in  $i_r$  and always no transient dc offset in  $i_m$ ).



# Parameter Sensitivity Tests #2 Closed-Loop Conditions

MPC+CTPSM



(a)

- The automatic resonant-frequency tracking technique starts from  $T_2$  and will last until  $T_6$ .
- 😊 MPC+GTSM always shows a significantly better transient performance over MPC+CTPSM, as transient oscillations can be observed under MPC+CTPSM.

# Parameter Sensitivity Tests #2 Closed-Loop Conditions

MPC+GTSM

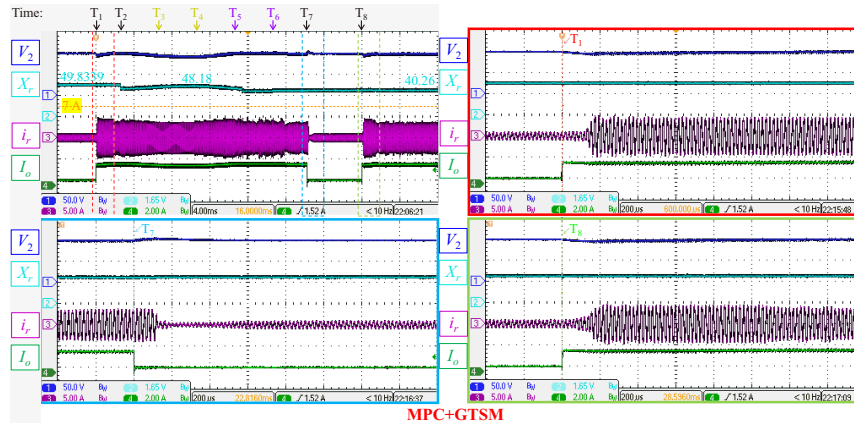


Figure 71: Experimental closed-loop online estimation of  $X_r$  and  $F$ . Transient waveforms for step load changes between 0.5 and 2 A are shown under (a) MPC+CTPSM and (b) MPC+GTSM.  $V_1 = 110$  V,  $V_2 = 100$  V,  $K_p^* = 0.08$ ,  $K_i = 0.002$ ,  $f_{s-n} = 50$  kHz,  $f_{s-i} = 52$  kHz, initial (incorrect) values of  $X_r = 49.8339$  and  $F = 1.4060$ .



# Contents

- ▶ Introduction
- ▶ Overview of Existing Modulation and Control Strategies
- ▶ Optimal Transient SPS Modulation for NR-DABC
- ▶ Trajectory-Switching Modulation for SR-DABC
- ▶ Generalized Trajectory-Switching Modulation for DABC
- ▶ Conclusions





# Main Research Contributions

- A set of unified equations are developed for governing all SPS-based OTPSM strategies of NR-DABC.
- A new condition enabling a full elimination of all transient dc offsets is introduced, which gave birth to the simplest and most effective OTPSM strategy (i.e., SS-OTPSM) for NR-DABC.
- SS-OTPSM+EMPC represents the first attempt in the related literature to discourse the co-optimization of transient modulation and controller designs to achieve dc-offset-free and ultrafast dynamics.
- A simple TSM is proposed to achieve oscillation-free dynamics in SPS-modulated SR-DABC.
- A powerful and generalized transient modulation approach, i.e., GTSM, is proposed for achieving oscillation-free and dc-offset-free dynamics in MPS-modulated SR-DABC/NR-DABC.
- We are the first to demonstrate the effectiveness of such optimized transient modulation strategies in a truly fast closed-loop controlled DABC.

**Table 7:** Comparisons of the proposed three transient modulation strategies.

Features & Capabilities	SS-OTPSM	TSM	GTSM
DC-offset Elimination	✓	✗	✓
Oscillation Suppression	✗	✓	✓
Compatibility with MPS Modulation	✓	✗	✓
Topological Compatibility	NR-DABC	SR-DABC	DABC



# Key Research Findings and Design Philosophy

## Research Findings

- ① Implementing OTPSM technology cycle by cycle in a closed-loop DAB system can significantly reduce transient dc offsets and high-frequency oscillations of the high-frequency-link currents, thereby indirectly increasing the control bandwidth and reducing the burden of controller design.  
**牽一發動全身，一子落滿盤活**
- ② OTPSM strategies are more suitable for use in combination with high-gain and fast controllers.  
**好馬配好鞍**
- ③ The deep integration and co-optimization of the Controller and Actuator (PWM Generator) can achieve truly optimal dynamic performance.  
**調控相融，珠聯璧合，相得益彰**

## Design Philosophy of OTPSM

- ① **Versatility:** OTPSM should preferably be compatible with different steady-state modulation strategies.
- ② **Simplicity:** OTPSM should preferably be easily implemented on a cycle-by-cycle manner.
- ③ **Robustness:** OTPSM should preferably be insensitive to changes in circuit parameters.



# References & Publications

## References Used in Presentation

All the sources and references used in this presentation are included in the following Ph.D. thesis.

C. Sun, "Optimized transient modulation and control strategies for bidirectional dual-active-bridge DC-DC converters," *HK PolyU (Pao Yue-Kong) Library*, 2023. (<https://theses.lib.polyu.edu.hk/handle/200/12668>)

## List of Publications

-  C. Sun, X. Jiang, J. Liu, L. Cao, Y. Yang, and K. H. Loo, "A unified design approach of optimal transient single-phase-shift modulation for nonresonant dual-active-bridge converter with complete transient dc-offset elimination," *IEEE Transactions on Power Electronics*, vol. 37, no. 11, pp. 13 217–13 237, 2022.
-  C. Sun, X. Jiang, L. Cao, and K. H. Loo, "Total suppression of high-frequency transient oscillations in dual-active-bridge series-resonant converter by trajectory-switching modulation," *IEEE Transactions on Power Electronics*, vol. 37, no. 6, pp. 6511–6529, 2022.
-  C. Sun, J. Liu, X. Jiang, L. Cao, Y.-C. Wang, J.-X. Shen, and K.-H. Loo, "Generalized multiphase-shift transient modulation for dual-active-bridge series-resonant converter," *IEEE Transactions on Power Electronics*, vol. 38, no. 7, pp. 8291–8309, 2023.



# Related Publications

-  R. Ding, X. Li, C. Sun, and A. K. Rathore, "Transient modulation based on the current coordinate system in nh3l-dab converter," in *2025 IEEE Industry Applications Society Annual Meeting (IAS)*, 2025, pp. 1–6.
-  R. Ding, C. Tang, C. Sun, X. Li, and A. Rathore, "Simplified state-trajectory analysis method for dual-active-bridge dc-dc converters," *Electronics Letters*, vol. 61, no. 1, p. e70267, 2025.
-  C. Tang, R. Ding, C. Sun, and X. Li, "Current-prediction based transient control of a dual-active-bridge converter with frequency modulation," in *TENCON 2024 - 2024 IEEE Region 10 Conference (TENCON)*, 2024, pp. 1324–1327.
-  R. Ding, S. Liu, C. Tang, X. Li, C. Sun, and S. Hu, "Modulation for step-load change of a neutralpoint-clamped hybrid three-level dual active bridge converter," in *2024 3rd International Conference on Power Systems and Electrical Technology (PSET)*, 2024, pp. 199–204.
-  H. Xu, S. Zhou, X. Li, H. Chen, and S. Hu, "Transient modulation for the step-load-change process in a dual-bridge series resonant converter," *Electronics*, vol. 11, no. 5, 2022.



# Related Publications

-  H. Xu, S.-Z. Zhou, X. Li, H. Chen, and S. Hu, "Fast transient modulation of a dual-bridge series resonant converter," in *IECON 2021 – 47th Annual Conference of the IEEE Industrial Electronics Society*, 2021, pp. 1–6.
-  Y. Tang, X. Li, S.-Z. Zhou, C. Sun, and G. Chen, "Comprehensive study of fast load modulation with volt-second balance in a dual-active-bridge converter," *IET Power Electronics*, vol. 12, no. 6, pp. 1357–1367, 2019.
-  C. Sun and X. Li, "Instantaneous current balance modulation for fast transient response in a dual-active-bridge converter," in *2018 IEEE International Power Electronics and Application Conference and Exposition (PEAC)*, 2018, pp. 1–6.
-  C. Sun, X. Li, and S.-Z. Zhou, "Transient current control for a step load change in a dual-active-bridge converter," *Electronics Letters*, vol. 54, no. 22, pp. 1290–1292, 2018.
-  Y. Zhang, X. Li, C. Sun, and Z. He, "Improved step load response of a dual-active-bridge dc–dc converter," *Electronics*, vol. 7, no. 9, 2018.



# Related Publications

-  C. Sun and X. Li, "Fast transient modulation for a step load change in a dual-active-bridge converter with extended-phase-shift control," *Energies*, vol. 11, no. 6, 2018.
-  S.-Z. Zhou, C. Sun, S. Hu, G. Chen, and X. Li, "Improved load transient response of a dual-active-bridge converter," in *2018 International Power Electronics Conference (IPEC-Niigata 2018 -ECCE Asia)*, 2018, pp. 370–374.
-  X. Li, S. Hu, C. Sun, and Y.-F. Zhang, "Asymmetric-double-sided modulation for fast load transition in a semi-dual-active-bridge converter," *IET Power Electronics*, vol. 10, no. 13, pp. 1698–1704, 2017.
-  S.-T. Lin, X. Li, C. Sun, and Y. Tang, "Fast transient control for power adjustment in a dual-active-bridge converter," *Electronics Letters*, vol. 53, no. 16, pp. 1130–1132, 2017.
-  X. Li and Y.-F. Li, "An optimized phase-shift modulation for fast transient response in a dual-active-bridge converter," *IEEE Transactions on Power Electronics*, vol. 29, no. 6, pp. 2661–2665, 2014.

# End of Presentation



**THANK YOU VERY MUCH  
FOR YOUR TIME AND ATTENTION !**

**Q&A**



**澳門科技大學**  
MACAU UNIVERSITY OF SCIENCE AND TECHNOLOGY

Dedication to practical studies,  
Enhancement of knowledge, Ability and Quality.

**意誠格物**